SCREAM 4: Super-elastic Continuum Robot for Endoscopic Articulation and Manipulation

Major Qualifying Project

Submitted By:

Hoang Do, Mechanical Engineering
Rositsa Mihaleva, Biomedical Engineering
Emily Minch, Biomedical Engineering
Ryan Tougas, Robotics Engineering, Electrical and Computer Engineering

Project Advisors:

Prof. Loris Fichera
Prof. Yuxiang Liu
Prof. William Michalson
Dr. Thomas L. Carroll (Brigham and Women's Hospital)

Worcester Polytechnic Institute

Aug 2021 - May 2022

Abstract

The goal of this project is to create a needle-sized continuum (i.e., continuously flexible) robot to enhance surgical access of the larynx during office-based endoscopic laser surgery. Existing instrumentation used for this procedure offers a limited range of articulation, rendering places such as the underside of the vocal folds inaccessible. We developed a robotic steerable laser fiber, equipped with three degrees of freedom, to overcome this challenge. The fiber, capable of bending, rotating and translating, is controlled by a compact, lightweight actuation unit which mounts on the endoscope handle. The steerable fiber is small enough (diameter: 1.1 mm) to be deployed through the operating channel of most clinical endoscopes. We characterized and verified the mechanical performance of the device experimentally as well as in simulation. Results indicate that our device increases gross tissue access by 150% compared to existing clinical instrumentation.

Introduction

Office-based surgeries are increasingly being used in the treatment of benign and pre-malignant tumors in the larynx. In the procedure, a flexible endoscope enters the nasal cavity to reach the larynx. An optical fiber is next passed through the working channel of the endoscope to deliver laser pulses to thermally ablate the tumors. Compared to operating room (OR) surgical treatments, office procedures present lower costs and complication rates [1]. However, prior studies have found that the reachable anatomy is limited by the restricted range of motion of the endoscope's distal tip [2]. This limits the physician's ability to reach certain locations within the larynx, including but not limited to the underside of the vocal folds. We propose a continuum (i.e., continuously flexible) robotic steerable sheath assembly, pictured in Fig. 1, that enables steering of the laser fiber independently of the endoscope motion. This assembly is controlled via a specially designed actuation unit that mounts on the endoscope handle. Through simulations and experiments, we demonstrate that our device provides increased anatomical access when compared to current clinical instrumentation.

This work is a continuation of a prior project exploring the feasibility of miniaturized continuum robots for laser surgery of the larynx [3]. We further the development of this project by improving the design of the actuation unit and by verifying its increased tissue access in simulation using three algorithms to generate reachability maps in two larynx models.

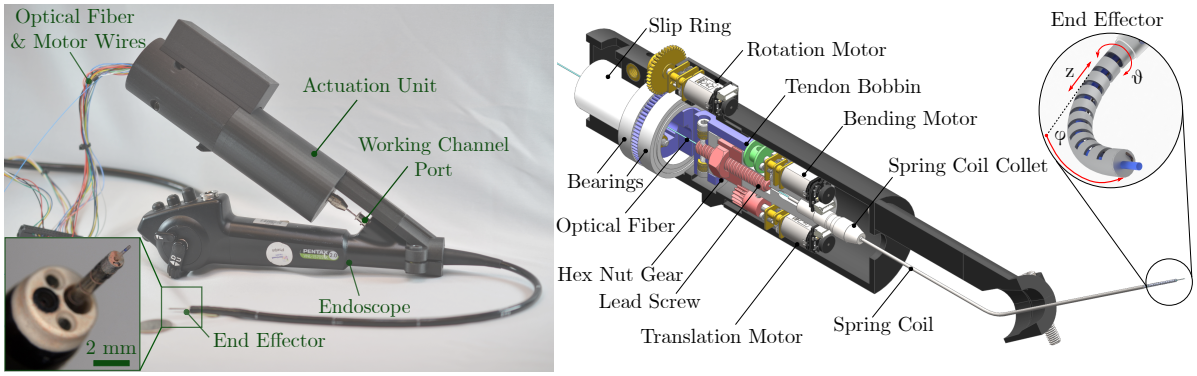

Figure 1: *Proposed steerable fiber. The physical device coupled to a hand-held flexible laryngeal endoscope (left). A rendering of the actuation unit (right).*

Design and Fabrication of a Steerable Optical Fiber for Laryngeal Laser Surgery

We designed a mechanism that provides distal steering to an optical fiber. In addition to steering, the mechanism provides fiber rotation and translation for a total of three degrees of freedom (DoFs) (as shown in Fig. 1). Our design involves two main components: a steerable sheath assembly and a mountable actuation unit, both shown in Fig. 1. The steerable sheath assembly comprises an optical fiber, Nitinol tendon, end cap, notched Nitinol wrist, and heat-shrink tubing to concentrically couple the assembly to the torsional rigid stainless steel spring coil. The wrist is tendon actuated (i.e. controlled by using the tendon). When the tendon is pulled, the wrist bends, similarly to the effect of the flexor tendon in a finger. When the tendon is released, the wrist returns to its straight pose, thanks to the super-elastic property of the Nickel-Titanium (i.e., Nitinol) material. The actuation unit contains off-the-shelf and custom 3D printed plastic parts, and three motors to independently control the three DoFs. It also houses a through-hole slip ring that transmits power and encoder signals between the static and moving portions of the unit, while allowing the optical fiber to pass through. Furthermore, the complete system (see Fig. 2) includes a user interface and a separate control unit and is designed to seamlessly integrate with the current office-based procedural equipment: the laser coupling system and endoscopy video processing unit.

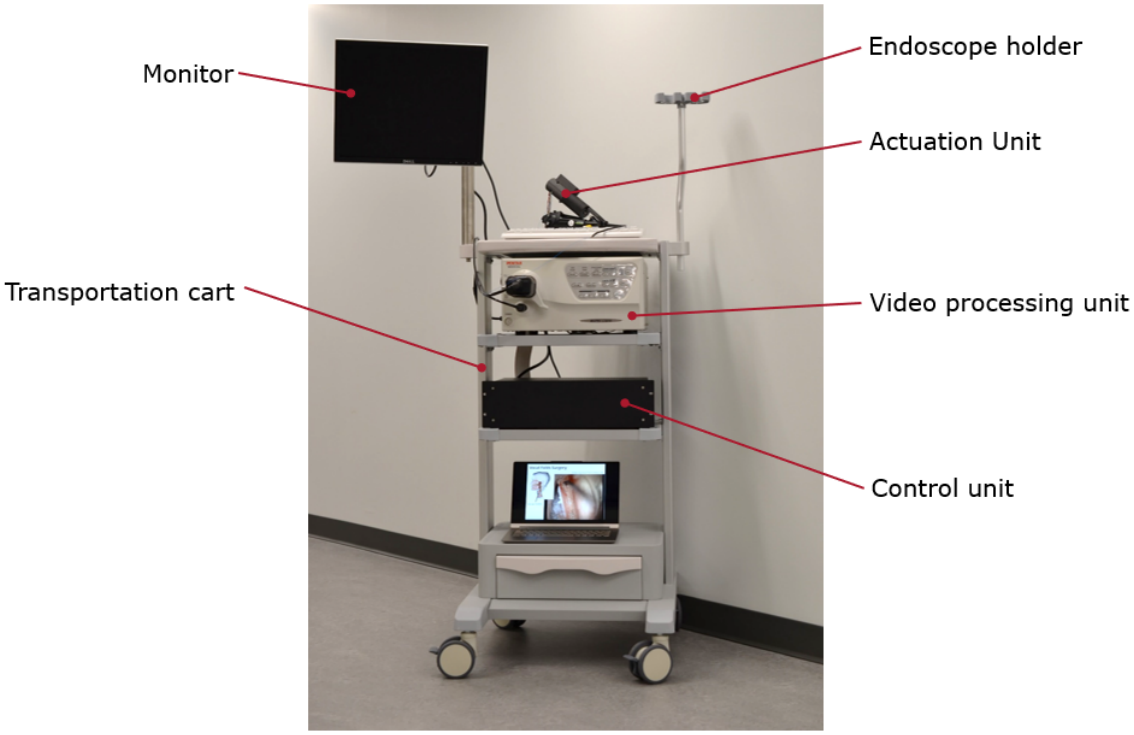

Figure 2: *Complete integrated SCREAM 4 system on a medical cart.*

Integration and Experimentation

The complete SCREAM 4 system is shown in Fig. 2. To transport our system conveniently, we purchased a TR900 endoscopy cart (Coriton Instrument Co., Shenzhen, China). This cart is capable of storing our devices, the Pentax video processing unit, and a monitor currently used by physicians for in-office procedures. To characterize the Nitinol wrist's deflection, we used the experimental setup shown in Fig. 3. The experiment protocol involved five trials of pulling the tendon using a linear slide in increments of 0.2 mm until the wrist was fully closed resulting in twelve data points per trial. The average results of the five trials are plotted in Fig. 4, showing a

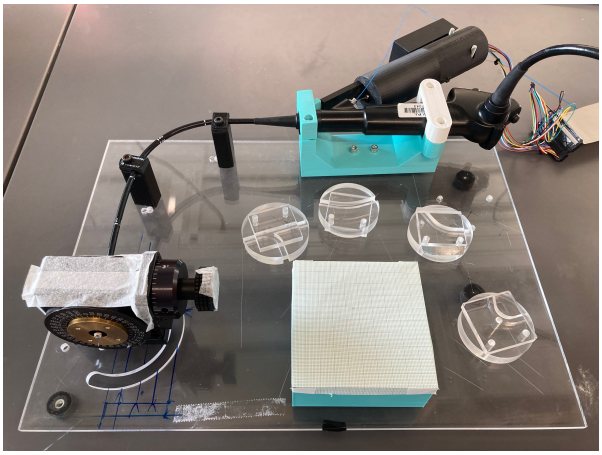

Figure 3: *Basic experiment setup used to evaluate the mechanical design.*

linear relationship between the tendon displacement and the bending angle of the steerable fiber. This is significant as it allows for implementation of a linear model that can be used to correlate tendon displacement with the resultant bending angle.

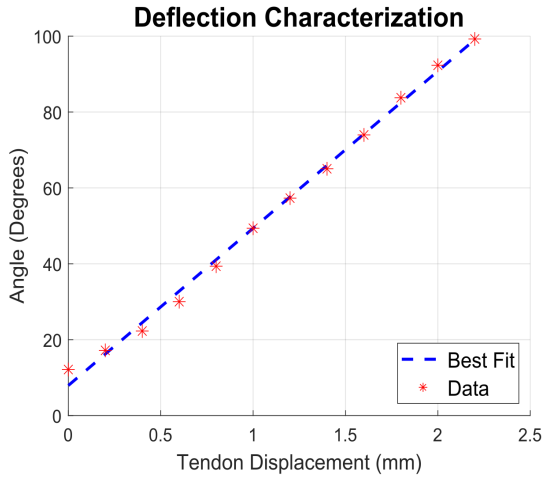

Figure 4: *Results of the kinematic evaluation experiments. For all values of tendon displacement, the standard deviation among the 5 trials was* $< 1°$.

To characterize the tissue accessibility of our new steerable fiber, we ran custom MATLAB (The Mathworks, Natick, MA, USA) simulations with two high-resolution 3D larynx models from microtomography scans of cadavers [4]. The scans were compiled into 3D stereolithography models. The simulations generated 10,000 random endoscopic configurations to establish the functional workspace using the Rapidly-Expanding Random Trees algorithm [5]. From each point, 1,000 virtual rays were emitted from the fiber tip to and were programmed to highlight the parts of the tissue that were in a direct line-of-sight. Results from the simulations, shown in Fig. 5 and Table 1, show that the steerable fiber more than doubles the amount of reachable anatomy compared to a traditional clinical fiber.

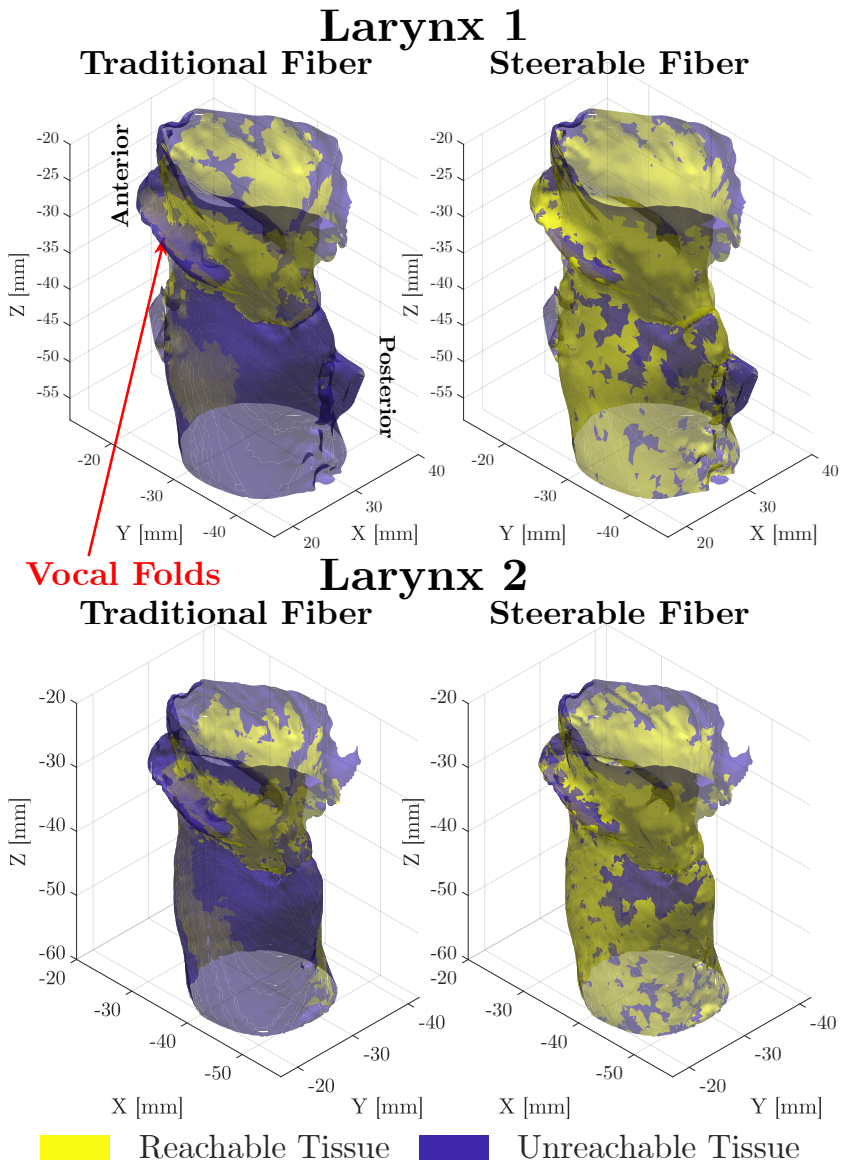

Figure 5: *Reachable tissue in two different larynx models. The "traditional fiber" refers to the non-steerable fiber, and the "steerable fiber" refers to our designed device.*

Table 1: *Tissue Coverage Estimated in Simulation*

	Traditional Fiber $\mathbf{cm^2}$	**Steerable Fiber** $\mathbf{cm^2}$
Larynx 1	8.99	22.22
Larynx 2	8.51	20.49

Discussion and Future Work

The experimental results suggest that our device can increase surgical access to the larynx with a demonstrated improved design of prototypes from prior MQP teams. To confirm the success of using steerable fibers in office-based larynx surgeries, we recommend further studies in simulation with a greater sample size of larynx models and different system parameter variations. More methods to optimize the design of the steerable sheath could be explored in the future to increase tissue reachability. More work is also needed to develop a user interface that provides the physician with ergonomic single-handed manipulation. Last but not least, the device needs to be clinically validated through cadaver experiments, for which our team has prepared a preliminary protocol.

ACKNOWLEDGEMENTS

This Major Qualifying Project was supported by Worcester Polytechnic Institute (WPI) and the Cognitive Medical Technology and Robotics Laboratory (COMET Lab). Thank you to the Robotics Engineering, Biomedical Engineering, Electrical and Computer Engineering, and Mechanical Engineering Departments for their support. We are appreciative of the National Institute of Health and WPI for providing us with the necessary funding.

We are grateful for the help of all our advisors for their instruction, especially Professor Fichera for holding our work to the highest quality and always being available to help. Thank you to Professor Michalson for providing expertise in electrical design and experimentation. Thank you to Professor Liu and his MQP team for their expertise with the laser-firing system. Thanks to Dr. Thomas Carroll and Dr. Elliana DeVore for providing clinical expertise to help us with device and simulation implementation. Thank you to Dr. Chris Nycz for providing us with feedback on the design of our device. Thank you to Professor Karen Troy for providing us with information on performing cadaver experiments at WPI. Thank you to Paula Moravek for helping provide us with blood-borne pathogen training to prepare for the cadaver experiments. Thank you to Pauline Joncas with the Robotics Engineering Department for helping us purchase the medical endoscopy cart. Thank you to Lisa Wall with the Biomedical Engineering Department for organizing Project Presentation Day. Thank you to Amanda Collins and the rest of the staff at the UMass Memorial University Campus Anatomy Laboratory for their help planning for the cadaver experiments. Thank you to all of the friends and family that have helped support us along the way. Last but not least, many thanks to Alex Chiluisa and Nicholas Pacheco for their continued mentorship, advice, and guidance as we developed our device.

Table of Contents

List of Tables

Table **Page**

List of Figures

Figure **Page**

CHAPTER 1

INTRODUCTION

Laryngeal tumors affect one in forty people worldwide [6]. The traditional way to treat laryngeal tumors involves surgery in an operating room [7] which requires the patient to undergo general anesthesia, leading to a high risk of complication and a long recovery time [3]. In recent years, office-based surgeries have grown in popularity to treat benign laryngeal tumors thanks to several benefits: the replacement of general anesthesia with topical anesthesia, the reduction of procedure expense for patients, the reduction of total procedure time, and higher otolaryngologist and hospital efficiency [1]. Additionally, by avoiding the use of general anesthesia, the treatment of benign larynx tumors becomes possible for certain patient groups, such as the elderly, who are normally at risk of complications from traditional operating room surgical procedures [2].

The typical setting for office-based laryngeal laser surgery is shown in Fig. 1.1(a). In the procedure, the operating physician passes a flexible laryngoscope through the nasal cavity and

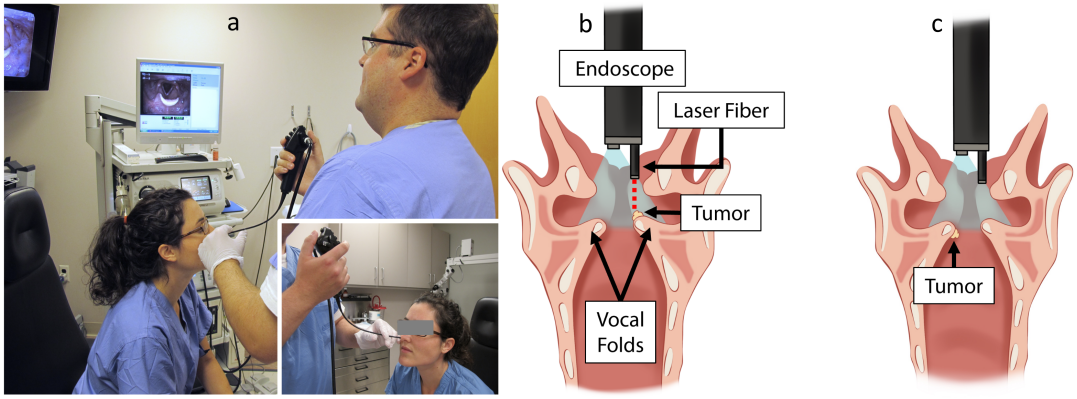

Figure 1.1: *(a) A typical office-based laser surgery setup. (b), (c) A diagram showing the distal tip of the laryngoscope [2].*

nasopharynx to reach the larynx. An optical fiber is passed through the working channel of the laryngoscope to deliver laser pulses at the site of the tumor. The distal tip of the laryngoscope also contains a camera, which provides visual guidance to the surgeon (Fig. 1.1(b)). The application of laser pulses thermally ablates the diseased tissues, which are re-absorbed and eliminated by the patient's body in a process known as *involution* [8]. This means that the ablated tissues become cellular debris, which are cleaned out by the body's white blood cells.

While office-based laser surgery can be used to treat a variety of benign tumors in the larynx [2], the procedure also has limitations. Currently, laser pulse delivery is limited by the bending capability of the endoscope's distal tip. This limits the physician's ability to reach certain locations within the larynx, including the underside of the vocal folds [3, 9] (Fig. 1.1(c)). Furthermore, the procedure can be disorienting for the physician due to the laryngoscope's current design which couples the camera and laser together; simply bending the endoscope steerable tip to aim the laser fiber would move the camera's field of vision as bending the endoscope steerable tip is the only way to aim the optical fiber. [3]. To overcome these constraints, we propose an actuated system that would allow the surgeon to steer the laser fiber independently of the endoscope's camera, minimizing disorientation, providing a larger reachable workspace for the physician in the larynx, and improving the utility of the in-office procedure.

This project is a continuation of the work completed by three prior MQP teams, who have explored the feasibility of miniaturized continuum robots for this application [3, 10, 11]. Through this project, we further the development of the prototype and system design created by the SCREAM 3 team [3] and verify the tissue reachability of the device in simulation, in order to prepare the project for a cadaver study.

1.1 Contributions of this Project

The contributions of this MQP project are:

- **A study on the benefits of side-firing laser fibers in office-based laryngeal surgery.** We performed computer simulations in three-dimensional models of the human larynx to characterize the extent of accessible anatomy afforded by side-firing fibers. Results of these simulations indicate that side-firing fibers provide more than two times more anatomical coverage than the forward-firing fibers currently in clinical use. These results corroborate the clinical utility of introducing fibers with variable aiming angles in office-based laryngeal laser surgery. This study extends the results previously reported by Chan *et al.* in [2]. *The results of this study were accepted for presentation at the Spring 2022 meeting of the American Broncho-Esophageal Association in Dallas, Texas. A manuscript reporting our findings is currently under consideration for publication in the Laryngoscope, a peer-reviewed medical journal.*

- **The design, fabrication, and testing of a new steerable fiber for office-base laryngeal surgery.** We performed a critical review of the steerable fiber built by the previous SCREAM MQP team, i.e., SCREAM 3 [3]), which led to the identification of improvements needed to advance the technology readiness level of the device. The new design we propose in this document improves over the prototype built by SCREAM 3 in three key areas (these points will be illustrated in detail in Chapter 3): (*i*) we performed a complete redesign of the actuation unit that avoids the cable tangling issues experienced by the SCREAM 3 prototype; (*ii*) we introduced a new, more torsionally stiff spring coil to provide rotation of the fiber, which mitigates the low transmission ratio observed in the SCREAM 3 prototype; (*iii*) we created a control box for the device to house its power supply and control circuitry; this control box can be installed on a standard clinical endoscopy cart, which we expect will facilitate the future deployment of the SCREAM device in a clinical setting. *Part of these results are reported in a manuscript currently under review for the 2022 IEEE International Conference on Intelligent Robots and Systems (IROS) in Kyoto, Japan, and available as a pre-print on arXiv [12].*

1.2 Paper Outline

The outline of this paper is as follows: **Preliminary Study: Evaluating the Limitations of Current Clinical Instrumentation** presents our study on the benefits of side-firing fibers in office-based laryngeal laser surgery. **Design and Fabrication of a Steerable Optical Fiber for Laryngeal Laser Surgery** describes the design process and the fabrication of our functioning prototype based on a critical review of SCREAM 3. **Integration and Experimentation** presents the set of experiments used to characterize the steerable mechanism and shows the proof of concept in simulation. **Discussion and Future Work** includes suggestions for the continuation of this project. **Broader Impacts** discusses the significance of this project beyond the scope of our laboratory from an engineering perspective.

CHAPTER 2

PRELIMINARY STUDY: EVALUATING THE LIMITATIONS OF CURRENT CLINICAL INSTRUMENTATION

We conducted a study in simulation via a custom MATLAB program (The Mathworks, Natick, MA, USA) that evaluated different device parameters to predict tissue reachability. The goal of our simulation experimentation is to obtain a better understanding of the larynx anatomy and the limitations physicians face during in-office procedures. Hard-to-reach regions inside the larynx include the two cavities immediately above the vocal folds and the inferior surface of the vocal folds, such as the tumor shown in Fig. 1.1(c) [13]. This experimentation supports the development of a steerable fiber to reach the unreachable regions in the larynx.

2.1 Simulation Methods

The simulation environment is shown in Fig. 2.1. Our simulations use seven different three-dimensional human larynx models that were generated from micro-computerized tomography scans, recently published by Bailly *et al.* [4]. The patient information for each larynx model is shown in Table 2.1. For these simulations, we used the software previously developed by Chan *et al.* [2]. In order to run the simulations, we prepared each larynx model by compiling the images into three-dimensional stereolithography (STL) models with a custom MATLAB (The Mathworks, Natick, MA, USA) script. Each STL model was composed of thousands of tiny triangular faces. The models were post-processed with the Quadric Edge Collapse Decimation filter in Meshlab [14] to reduce the number of triangular faces, which subsequently reduced the computation time of the simulations.

The endoscope simulated in this study is the Pentax VNL-1570STK14, a nasal flexible laryngoscope with a working channel of 2 mm and a diameter of 4.9 mm. In its typical orientation,

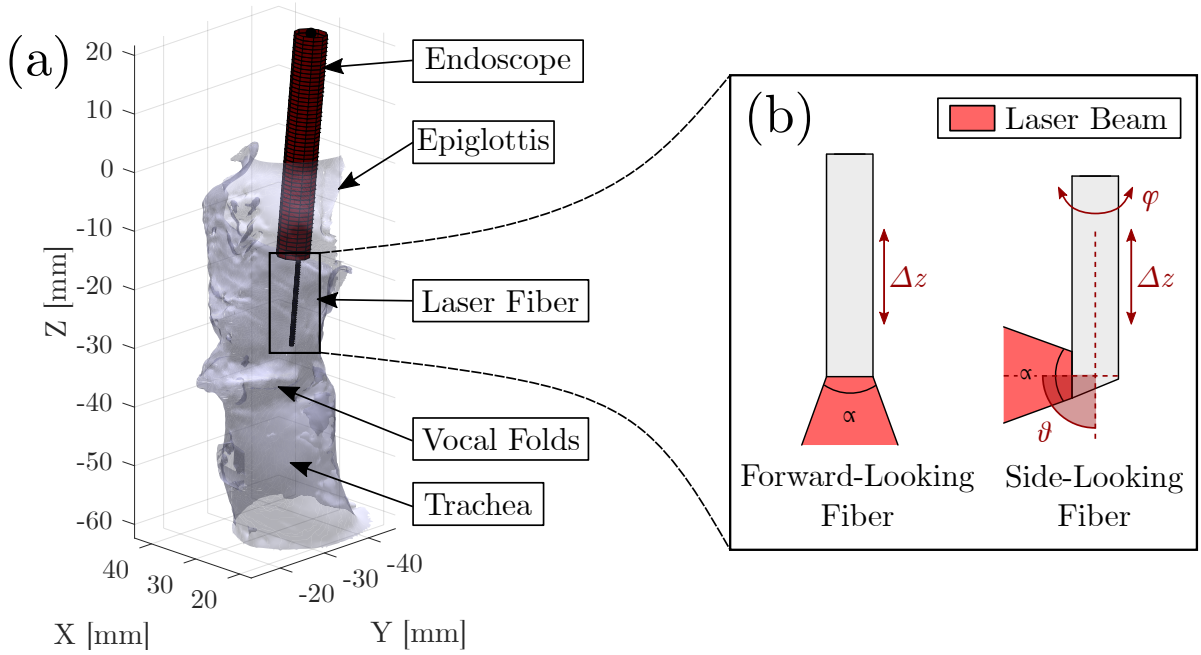

Figure 2.1: *Firing angle simulation environment, reproduced from Chan et al. [2].*

Table 2.1: *Patient information, reproduced from Bailly [4].*

Larynx	Gender	Age[y]	$V_{vox}[\mu m^3]$
L_1	F	86	45^3
L_2	M	94	25^3
L_3	F	82	25^3
L_5	F	85	13^3
L_6	F	89	13^3
L_7	M	81	13^3
L_8	M	89	13^3

the tip of the camera is located over the right vocal fold and the tip of the laser fiber is located over the left vocal fold as it was shown in Fig. 1.1(b) in the previous chapter. The range of motion of the endoscope, as determined by the project's clinical advisor, Dr. Carroll, is -120° to 120° for bending (constant curvature) and -100° and 100° for rotation. Currently, for in-office procedures, rotation and translation can only be achieved by the physician performing hand and arm movements while bending is performed by the endoscope's tip.

Using a sample-based motion planning algorithm, Rapidly-Exploring Random Trees (RRT), we generated 10,000 points of endoscope configurations inside each larynx model. From each point, a ray casting algorithm was used to mimic a conical laser beam, which consisted of 1,000 virtual rays cast from the tip of the fiber. All fibers used in the experiment have a diameter of 0.6 mm and are assumed to emit a cone-shaped beam with a divergence angle α = 40°. For each

ray, the Möller–Trumbore ray-triangle intersection algorithm was used to detect the reachable faces of the STL larynx model. If an STL face was too far from the tip of the laser fiber (> 3 mm), it was not marked as reachable. This is because the tissue would not be irradiated with a sufficient power density to ablate due to the divergence of the laser beam at this distance. Due to the anatomical differences of the cadavers, different simulation parameters had to be used for each larynx model. These parameters were chosen for each specific larynx due to their anatomical differences and to decrease the runtime of the simulations. As shown in Table 2.2, the dq, the step size between each randomly chosen point, varied between each larynx. For more details about dq, readers are referred to [5].

2.2 Comparing Firing Angles

We simulated four different laser firing approaches: a traditional forward-looking fiber, emitting light at angle $\theta = 0^{o}$, and side-looking fibers at $\theta = 45°$, $70°$, and $90°$. The simulation environment and laser-firing conditions are shown in Fig. 2.1(a) and Fig. 2.1(b), respectively.

Table 2.2: *Reachable area results according to laser firing angle.*

Larynx	dq	0^{o} [mm^2]	45^{o} [mm^2]	70^{o} [mm^2]	90^{o} [mm^2]
L_1	0.06	992.95	1220.42	1465.98	1545.11
L_2	0.06	848.15	1252.65	1445.52	1502.05
L_3	0.03	296.34	447.43	504.34	526.89
L_5	0.03	189.73	383.64	479.36	504.88
L_6	0.06	243.06	492.01	585.70	621.69
L_7	0.06	326.20	492.90	595.92	661.27
L_8	0.06	150.91	312.47	424.07	460.68

Table 2.3: *Reachable area percentage increase results.*

Larynx	0^{o}-45^{o} Increase [%]	0^{o}-70^{o} Increase [%]	0^{o}-90^{o} Increase [%]
L_1	32.19	58.82	67.40
L_2	47.66	70.40	77.08
L_3	50.99	70.19	77.80
L_5	102.20	152.65	166.10
L_6	102.42	140.97	155.78
L_7	51.10	82.69	102.72
L_8	107.06	181.01	205.27
Mean Percent Increase	76.91	116.32	132.51
Standard Deviation	29.64	47.92	53.86

As shown in Table 2.2, it was found that the angled fibers, 45^o, 70^o, and 90^o, allowed for more access to larynx tissue when compared to the traditional forward-firing laser fiber, 0^o, with the angled fiber 90^o showing the largest increase in tissue reachability. The mean increases, as shown in Table 2.3, were 76.91%, 116.32%, and 132.51% for 0^o to 45^o, 45^o to 70^o, and 70^o to 90^o respectively. The simulation results are shown in Fig. 2.2 for 7 larynx models. As shown in the column on the left, when using a forward-facing fiber, there is typically an unreachable gap on the right vocal fold that a 90^o side-firing fiber can restore. It was concluded in simulation that the 90^o side-firing fiber provided greater anatomical access to the larynx tissue than a traditional forward-facing fiber. While this may be true in simulation, this finding needs to studied experimentally to understand the benefits or risks of using side-firing fibers.

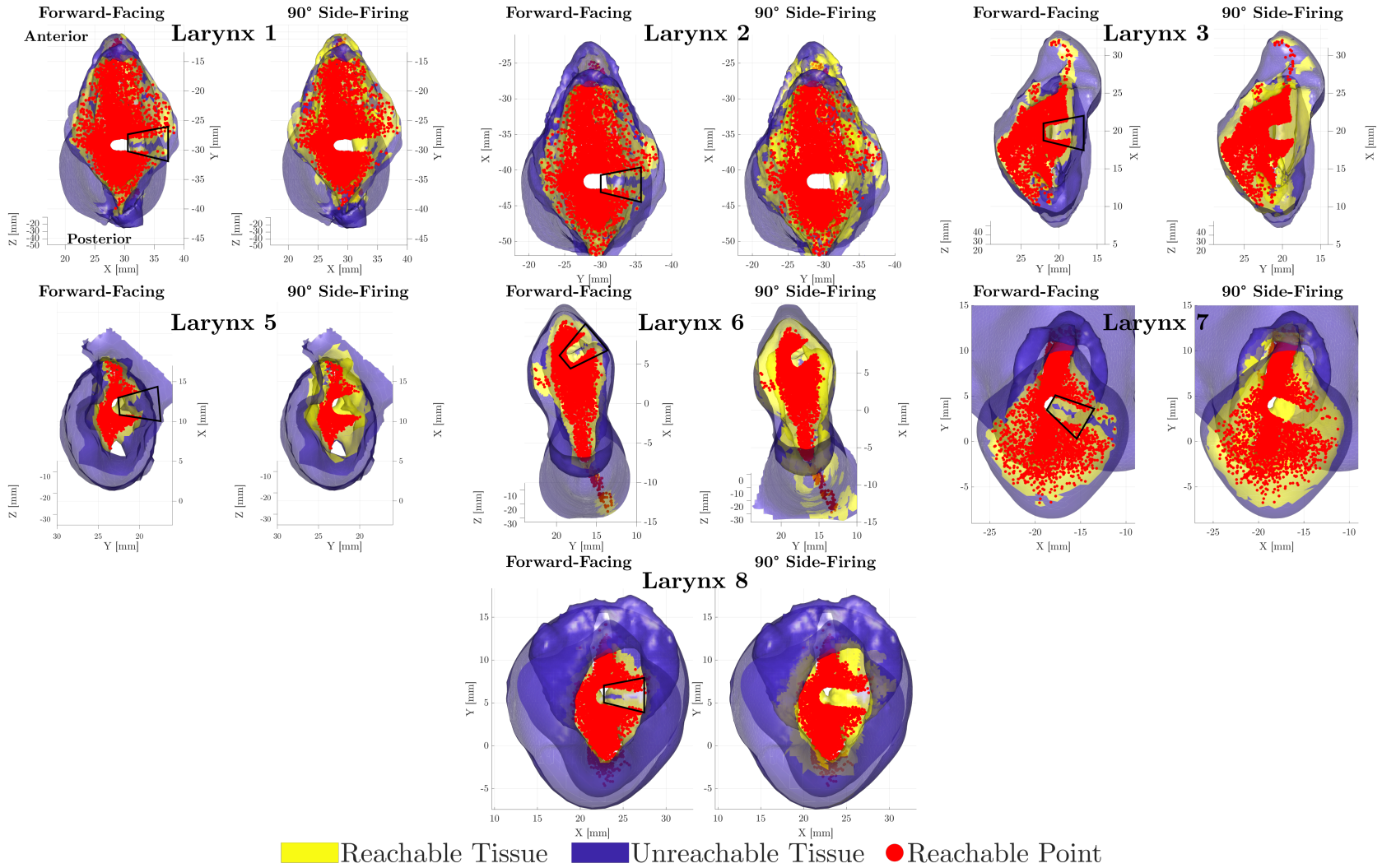

Figure 2.2: *Axial view of firing angle simulation results comparing a traditional forward-facing fiber with a 90° side-firing fiber. The red points represent the randomly generated endoscopic configurations, the yellow tissue represents reachable tissue, and the blue tissue represents unreachable tissue. In each model, a gap in the group of reachable points was found on the right side of the larynx. The likely cause of such a gap is the limited dexterity of the endoscope, as it was observed in [2]. For the sake of traceability, numbering of the different larynx models is the same as in [4]. Larynx 4 was not used in this study, as the corresponding set of images in [4] only captures a restricted portion of the glottic area (i.e., the anatomy surrounding the vocal folds), and it is therefore not suitable for this study.*

CHAPTER 3

DESIGN AND FABRICATION OF A STEERABLE OPTICAL FIBER FOR LARYNGEAL LASER SURGERY

The preliminary studies illustrated in Chapter 2 suggest the utility of introducing optical fibers with angled tips in laryngeal laser surgery. In this chapter, we present the design for our proposed robotic actuating device to provide optical fiber steering in laryngeal surgery. Our prototype involves a customized spring coil, actuation unit, and control unit, which built upon and improved the iteration by SCREAM 3.

3.1 Critical Review of the SCREAM 3 Steerable Optical Fiber

Before presenting our design, we briefly review the work performed by the SCREAM 3 MQP [3] which provides the foundation for this project.

3.1.1 Original Design Requirements

Through an interview with the clinical adviser of this project, Dr. Thomas Carroll, SCREAM 3 identified several functional requirements (FRs) and non-functional requirements (NFRs) for their steerable system design. In short, the FRs specify the design parameters that would allow the actuation unit, which houses the motors, to provide three degrees of freedom (DoFs) to the end effector, i.e., the laser fiber distal tip: deflection, translation, and rotation. The FRs generally concern the designs of the steerable sheath assembly and the actuation unit. The NFRs refer to the requirements not affecting the DoFs' behaviors but the human interaction with the design. The NFRs generally affect the designs of the user interface, control unit, and the system as a whole. The requirements are as follows [3]:

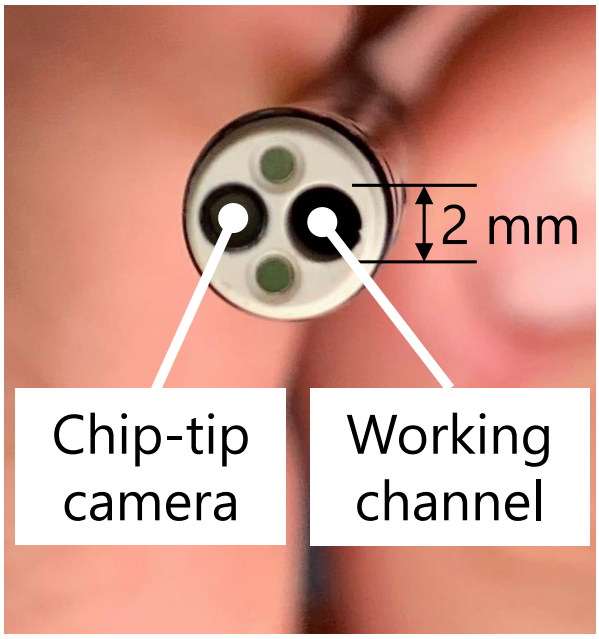

Figure 3.1: *View of endoscope's distal end, showing its chip-tip camera and 2 mm diameter working channel. Reproduced from [3].*

Functional Requirements (FRs):

- **FR 1:** The steerable mechanism must be smaller than 2 mm in diameter to fit into the working channel of the endoscope (see Fig. 3.1).
- **FR 2:** The steerable mechanism must be able to bend 90°.
- **FR 3:** The steerable mechanism must be able to bend with a radius smaller than 14 mm, which is the current bending radius of the endoscope distal tip.
- **FR 4:** The steerable mechanism must be able to translate the laser fiber approximately 1-2 cm in and out of the endoscope working channel.
- **FR 5:** The steerable mechanism must be able to rotate the laser fiber 360°.

Non-Functional Requirements (NFRs):

- **NFR 1:** The need to integrate a robotic system with the existing endoscope handle in a way that is intuitive and easy for the physician to operate.
- **NFR 2:** Controls that enable one physician to complete the procedure alone.

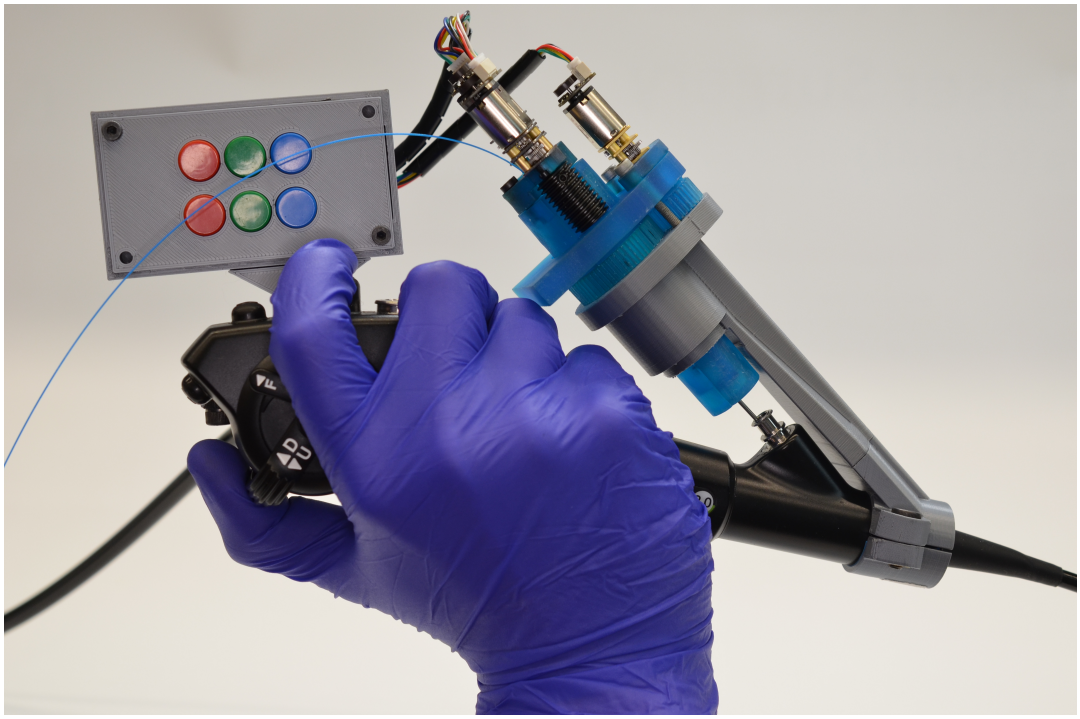

Figure 3.2: *SCREAM 3 actuation unit and user interface mounted on an endoscope [3].*

3.1.2 SCREAM 3 Achievements

Regarding the design requirements, SCREAM 3 achieved FRs 1, 3, 4, 5 and NFR 1. Fig. 3.2 shows SCREAM 3's mountable actuation unit that controls the steerable mechanism and a mountable user interface. These components fulfilled FRs 4, 5, and NFR 1. To achieve FRs 1 and 3, SCREAM 3 designed and fabricated a steerable wrist. This wrist can bend and steer the laser fiber independently of the endoscope tip, providing the physician the ability to access greater areas of tissue with more ease and refined motion.

This wrist design was that of a laser notched Nitinol tube, as seen in Fig. 3.3. Nitinol, a Nickel-Titanium alloy, was selected for this application thanks to its super-elastic properties. When tendon displacement is positive, i.e., when the tendon is pulled, (see Fig. 3.3), the wrist containing a laser fiber would bend. When the tendon is released, the super-elasticity allows the wrist to revert to its original "straight" configuration. Compared to a more traditional pin-and-socket hinge, the notched tube configuration would allow the end effector to navigate within narrow passages, such as the larynx [15].

The previous team produced four physical wrists, two of which were used by us this year (see Table 3.1). Throughout this project, Wrist 1 was used for the rotation and translation characterization experiments in section 4.2. Unfortunately, this wrist broke during an experiment trial, leading us to use Wrist 2 for the bending characterization experiment and the verification simulations explained in later sections.

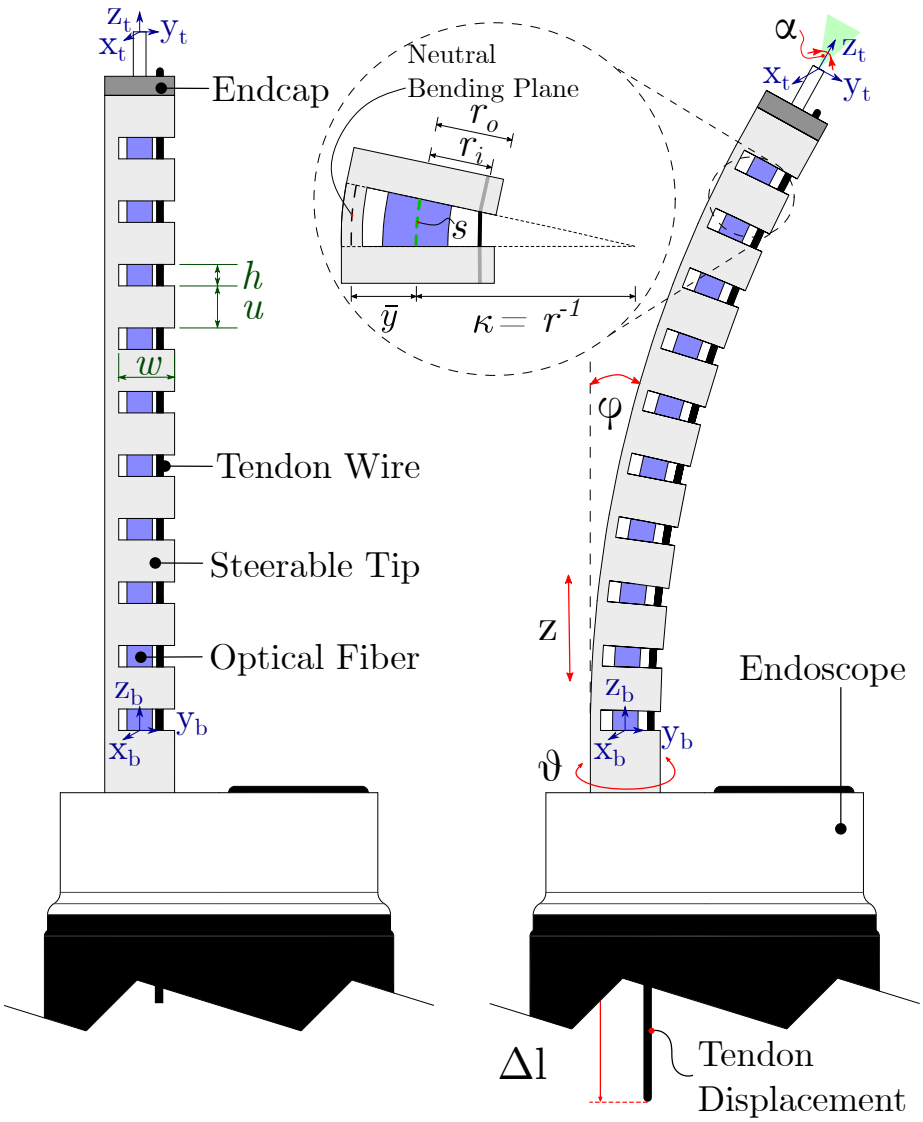

Figure 3.3: *Diagram of notched tube.*

Table 3.1: *Design parameters of the notched wrist.*

Parameter	Wrist 1	Wrist 2
Number of notches, n	10	10
Notch width, w (mm)	0.94	0.94
Notch spacing, u (mm)	0.66	1.31
Notch height, h (mm)	0.34	0.19
Bending radius, R (mm)	3	8
Steerable length, L (mm)	10	15

3.1.3 SCREAM 3 Areas of Improvement

Regarding the design requirements, SCREAM 3 did not achieve FR 2 and NFR 2. The previous device was only capable of bending 80°, 10°short of FR 2 target. While a UI was developed to address NFR 2, it was not verified within a clinical setup.

Beyond improvements directly tied to the established requirements, there were other areas within the design and implementation our team determined necessary to improve.

Spring Coil SCREAM 3 did a study on the use of spring coils to connect the steerable wrist with the actuation unit. A spring coil is a flexible hollow tube that is torsional, compressional, and extensional rigid. However, according to feedback from the physician, the rotation of the fiber was unpredictable, which was due to the coil selected by SCREAM 3 (Spring coil 1 in Table 3.2). Though spring coils 1 and 3 have a clockwise (CW) ratio closest to 1, their counterclockwise

Table 3.2: *Ratio of rotation transmitted in each direction of rotation with the tip bent at 0 degrees, adopted from SCREAM 3 [3].*

Spring Coil Number	Product Name	CW Ratio	CCW Ratio
1	SG-052-013-44	0.97	0.42
2	OLYMPUS FB-211D	0.61	0.51
3	PENTAX KW1806S	0.92	0.53
4	ConMed 100507	0.81	0.56
5	SG5-052-010-016-120	0.18	0.07

(CCW) ratio is low. This difference is potentially due to the winding direction of the filars making up the coil. In practice, this difference between the two ratio of a coil leads to snapping behavior of the spring coil. As the spring coil rotates within the endoscope working channel, elastic energy is stored within the coil; the coil appears stationary visually. When the torque in the coil exerts a force higher than the static frictional force between the coil and the working channel wall, the energy is released, causing the coil to rotate by a larger-than-expected amount. Because of these issues, we see torsional rigidity as one area of improvement for SCREAM 4.

Actuation Unit Regarding the design of the actuation unit (see Fig. 3.4), there were problems that impacted both the operation and ease-of-assembly of the device. The most critical design problem was that bending and translation DoFs were coupled. The impact of this was that translation of the wrist modified the displacement of the tendon, changing the resultant bending angle. As shown in Fig. 3.4, when motor 2 translates the spring coil outwards, motor 3 is not actuated, meaning that the length of tendon wire within the spring coil remains unchanged. This causes the tension in the tendon wire to increase, leading to bending of the wrist without actuating motor 3. Vice versa, when the wrist is bent and the spring coil is translated inwards, the wrist would unbend due to the decrease in tension within the tendon wire. Additionally, there was no compensation present in the software to correct this behavior, meaning that the user

would need to keep track of the tendon tension to ensure it remained approximately constant during translation.

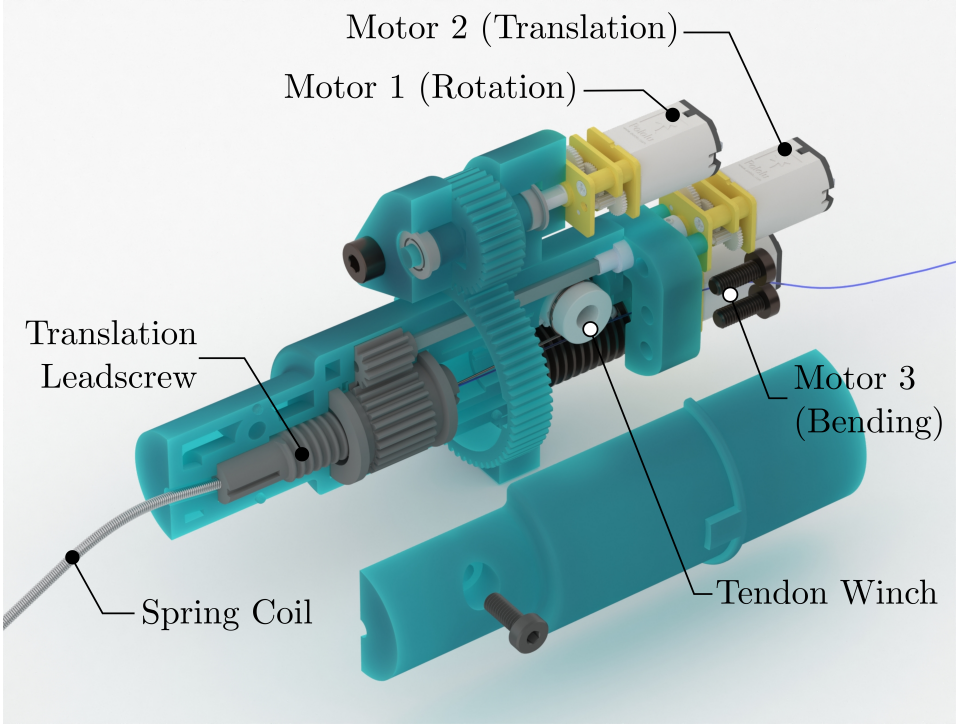

Figure 3.4: *Exploded rendering of the SCREAM 3 actuation unit [3].*

Table 3.3: *The relationship between the motors and the DoFs for SCREAM 3. A checkmark represents that the motor will move the tip in the corresponding DoF.*

	Deflection DoF	Translation DoF	Rotation DoF
Deflection Motor	✓	✓	
Translation Motor	✓	✓	
Rotation Motor			✓

Bending was also unreliable as the actuating tendon was not well guided by the actuation unit. The tendon winch had no walls to restrain the tendon, and as a result, the tendon would often fall off the groove and get caught within the design. The spring coil was coupled to the lead screw via superglue, which made modifications of the steerable sheath assembly a time-consuming process.

Additionally, the cables output from the motors were statically connected to the control circuitry. Thus, when the unit was rotated, the cables from motors 2 and 3 would begin to twist and disconnect.

3.2 Updated Design Requirements

With the areas of improvement that we identified, beside adopting all the FRs and NFRs identified by SCREAM 3, we added three requirements.

- **FR 6: Be able to rotate the end effector with high clockwise and counterclockwise ratio.** We added this requirement to tackle the issue associated with the spring coil in SCREAM 3. Achieving this FR would provide a more predictable rotational control of the laser fiber for the user.

- **FR 7: Be able to control each DoF independently of each other.** This requirement would help solve the problem of coupled translation and deflection DoFs. The solution should allow the end effector to change the pose only in the direction that the physician is actuating. The ideal relationship between the motors and the DoFs are shown in 3.4

Table 3.4: *The relationship between the motors and the DoFs. A checkmark represents that the motor will move the tip in the corresponding DoF.*

	Deflection DoF	Translation DoF	Rotation DoF
Deflection Motor	✓		
Translation Motor		✓	
Rotation Motor			✓

- **NFR 3: Be able to switch the steerable sheath assembly quickly in between procedures.** This NFR would help reduce the time we need to change the sheath assembly for our project in the short term and in between procedures in a clinical environment. This NFR was necessary due to the time-consuming process we went through to prepare SCREAM 3 actuation unit and steerable sheath assembly for a demonstration.

3.3 SCREAM 4 Design Solution

3.3.1 Spring Coil

The main improvement made to our version of the steerable sheath assembly is the spring coil. This spring coil needs to satisfy the existing FR 1 and the new FR 6. For our system, we selected the hollow cable ACT ONE Standard (Asahi Intecc Medical Components, Seto, Aichi, Japan) with an outer diameter of 1.37 mm (satisfying FR 1) and an inner diameter of 0.81 mm. This spring coil, made of Stainless Steel 304, possesses a high torque transmission, as well as a high flexibility and kink resistance. ACT ONE coils can be further customized to reduce the friction with the inner lumen of the endoscope working channel by using a coating or to improve the integration with the other components of the assembly by laser welding the coil to the notched tube or cutting the coil to a specified length. However, due to long manufacturing lead time and

the notion that the added benefits are not part of our design requirements, we decided to obtain readily available samples instead of getting customized coils. To evaluate the performance of this new spring coil against FR 6 and the coil used in SCREAM 3, we performed several experiments which we report on in section 4.2.

3.3.2 Actuation Unit

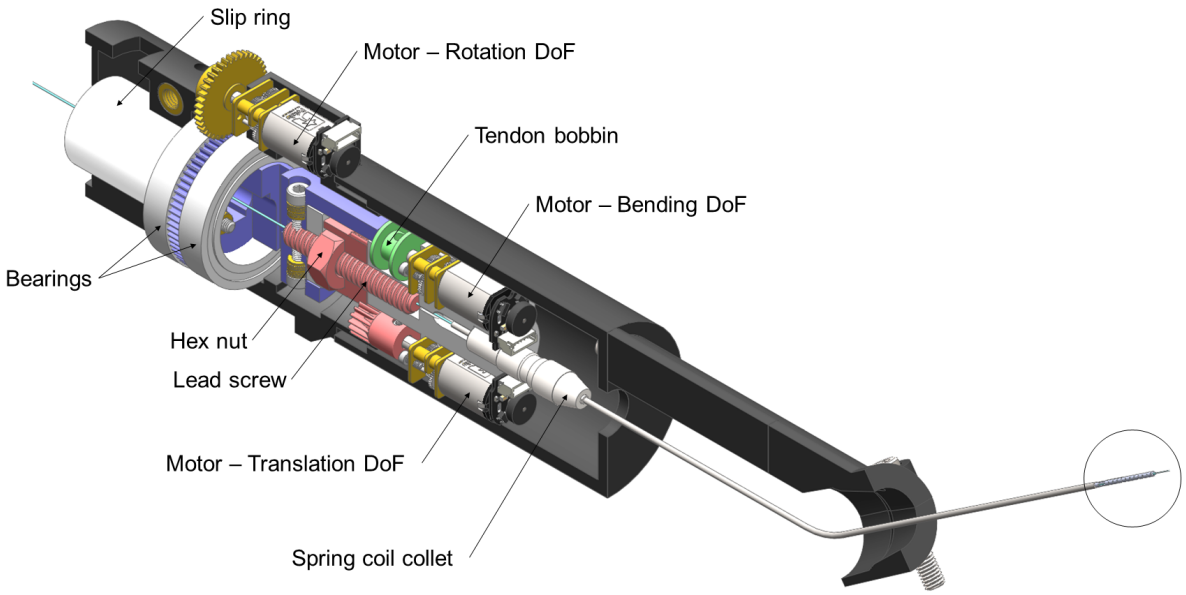

Figure 3.5: *Rendering of SCREAM 4 actuation unit with callouts indicating the main components.*

The main motivations for improving SCREAM 3 actuation unit are to achieve FR 7 and to avoid cable tangling. When designing a new unit (Fig. 3.5), we employed a nested design that would translate the deflection motor in the same displacement as the tip, ensuring that the tension in the tendon wire is unchanged. In the same way, to maintain independence between the three DoFs, bending and translation motors rotate in the same direction when the rotation motor is actuated.

For the second issue of cable twisting, we investigated using a slip ring, which enables the transmission of power and signals from the static to the moving portions of an assembly. For this design, we used a slip ring with a through-hole that would allow the optical fiber to pass through the actuation unit with minimal twisting and bending.

Furthermore, to tackle NFR 3, we used a spring coil collet, adapted from a pin vise, to affix the steerable sheath assembly to the actuation unit. This collet removes the need to use superglue to attach the spring coil to the actuation unit. The replacement of the steerable sheath assembly can now be performed by simply loosening the collet by unscrewing the tip.

Transmission mechanisms To bend the steerable fiber, we pull the Nitinol tendon using a motor with a 380:1 gear ratio. The tendon is wound up on a bobbin (shown in green in Fig. 3.6) affixed to the shaft of the motor. Translation is created via a lead screw and nut mechanism that converts the rotary motion of another 380:1 DC motor to linear translation. The encased hex nut moves linearly along the stationary lead screw, at a rate of 1.60 mm per turn. The design has a mechanical limit of 17.0 mm for the translation distance. Rotation uses a 298:1 motor connected to a brass gear, which interfaces with a custom gear (shown in blue in Fig. 3.6). The gear ratio between the motor shaft and the spring coil collet is 7:4.

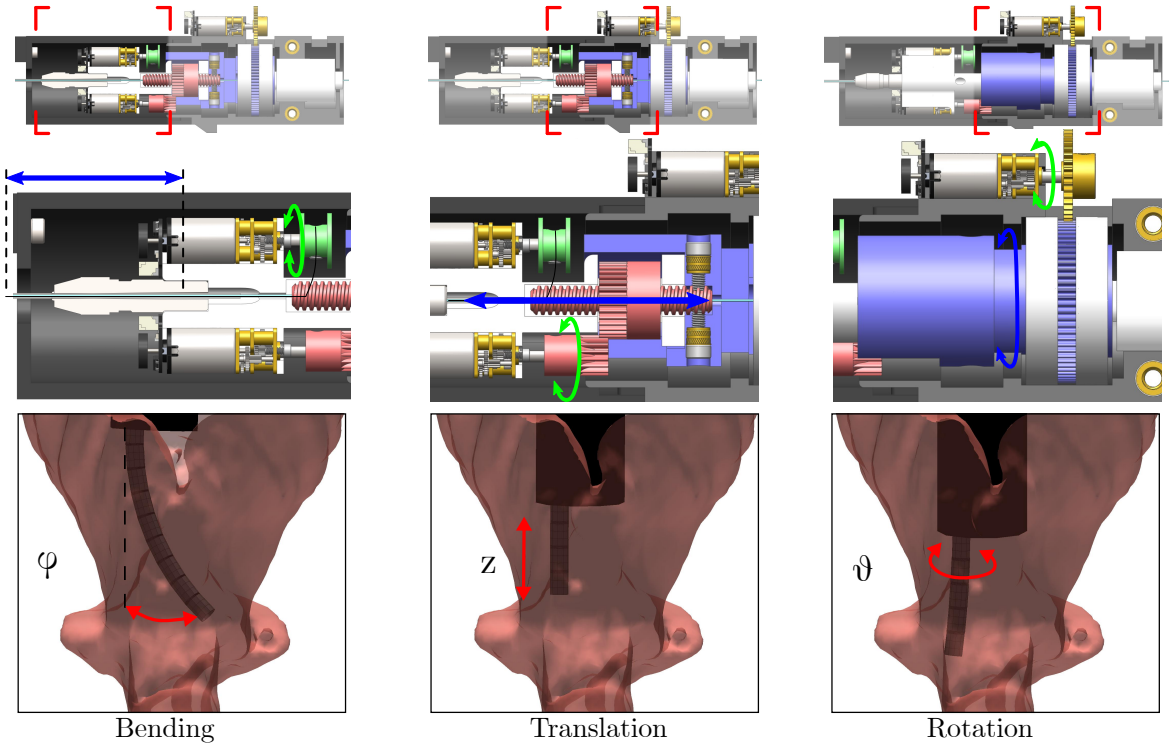

Figure 3.6: *Functional illustration of the actuation unit (from top: section view of the unit, detailed view of the actuated DoF, and the resulting probe motion within a larynx rendering).*

3.3.3 Control Unit

One feature of the SCREAM 3 design was that its microcontroller was placed within the button panel housing, mounted on the endoscope. The result of this assembly is that it is compact, and the button panel only needs to be directly connected to power to begin operation. However, the result of this design was that the compact microcontroller size was prioritized, to minimize bulkiness and heaviness of the endoscope (see Fig.3.7).

Our team proposed that moving the microprocessor off of the endoscope and to an external unit would remove the size restriction of the microcontroller, allowing for larger and more capable replacements. Furthermore, other associated control circuitry can also be moved to an external

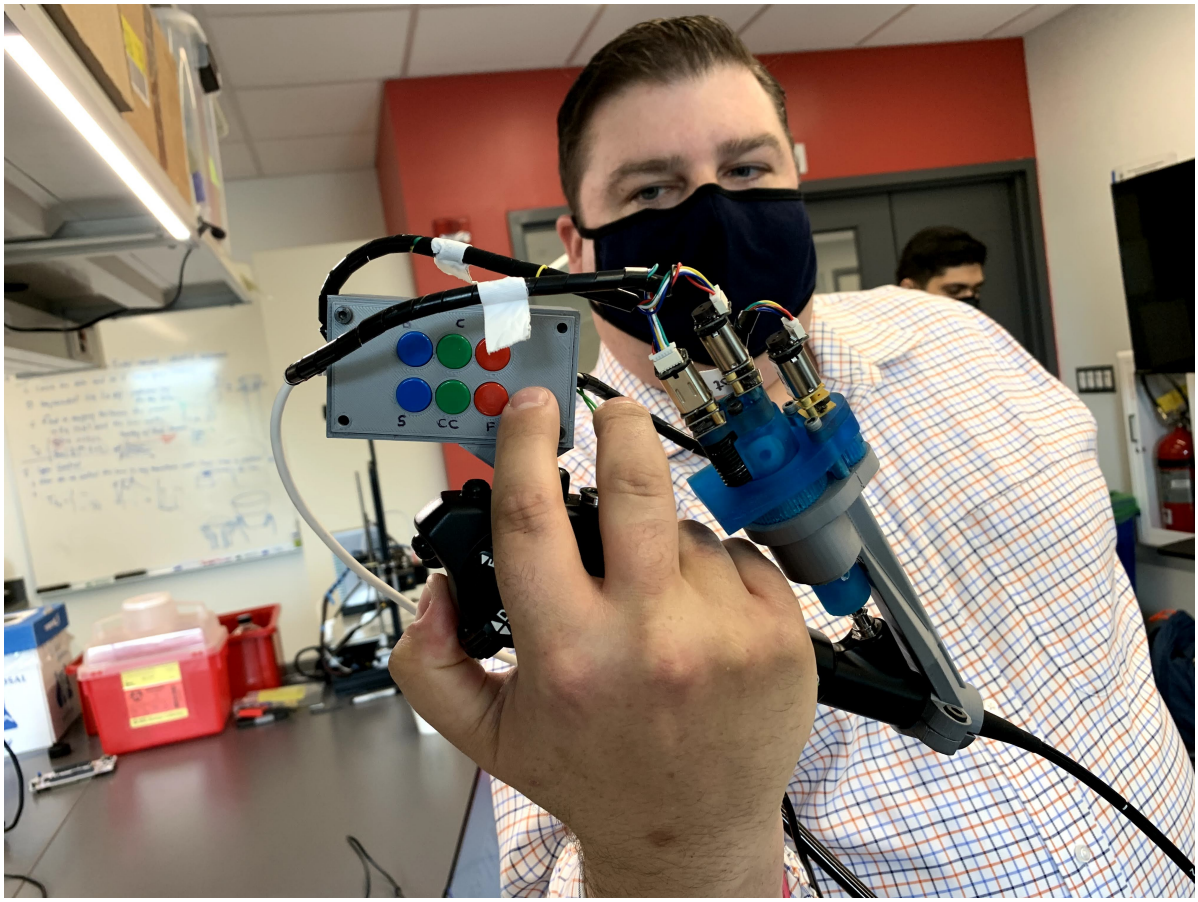

Figure 3.7: *Dr. Carroll holding the endoscope with the mountable button control panel by SCREAM 3.*

unit, so the only necessary electrical components on the endoscope remain: the motors, and UI electronics (buttons, encoders, potentiometers). These external electronics can then be combined with a power supply into a chassis that acts as the singular controller of the actuation unit. This also eliminates the need for an external lab power supply, used to power the SCREAM 3 device. The actuation unit will be connected to the custom control unit via a cable, which now passes through the user interface signals, motor power, and motor encoder outputs.

With these new design liberties, our team decided on the Nucleo F334R8 microcontroller. The Nucleo has 43 non-latching GPIO pins, all capable of being configured as digital in/out, and analog in. Compared to the ESP32's 16 GPIO pins, some of which are latching, the Nucleo offers much more control options to improve our design. The almost-tripling increase in total GPIO pins allows for the option of adding more motors and control options. Our team decided on configuring the Nucleo to handle a maximum of 6 motors, and 13 digital inputs. This abundance of input and output options allows for rapid prototyping without the need for physical change on the control end. Only the software needs to be configured to fit the specific needs.

The power supply in the control unit directly outputs 6V, matching the input voltage of the

motors; the most power-hungry components of our assembly. Furthermore, the power supply is designed to safely handle the worst-case-scenario that all 6 motors would stall, creating approximately 6.6A (1.1A each) in total. Nonetheless, each motor is fused, with a slow-blow 800mA fuse to ensure stall is never reached. The power supply also contains 3.3V and 5V regulators, necessary for the debouncing and inverter circuitry for the digital inputs (3.3V), and powering the Nucleo (5V). The motors are controlled using H-Bridges, while the Nucleo is also capable of controlling the H-bridge chip enable, allowing for the use of pulse width modulation. Lastly, a 2 x 20 female header pin is used as output to connect to the actuation unit. The schematics for our control unit (control and power schematic) are located in Appendix C.

CHAPTER 4

INTEGRATION AND EXPERIMENTATION

4.1 Integration

This chapter covers the process of building our physical unit, performing mechanical characterization experiments to test its performance, conducting simulations in MATLAB to test wrist coverage under varying parameters, and our preparations for cadaver studies. The complete SCREAM 4 system is shown in Fig. 4.1. In order to transport our system conveniently, especially for the cadaver study, we purchased a TR900 endoscopy cart (Coriton Instrument Co., Shenzhen, China). This cart is capable of storing our devices, the Pentax video processing unit, and a monitor currently used by physicians for in-office procedures.

Steerable Sheath Assembly The steerable sheath assembly consists of an optical fiber, a Nitinol tendon, an end cap, a Nitinol wrist, a heat-shrink sleeve, and lastly an ACT-ONE spring coil (See Fig. 4.2). The first step to make the assembly is to pass the Nitinol tendon through the loop in the end cap, leaving two segments of tendon equal in length. The tendon segments are then passed through the Nitinol wrist, so that the 'stem' of the end cap fits into the tip of the wrist. The tendon segments are next passed through the spring coil, so that the end of the wrist makes contact with the tip of the spring coil. The heat-shrink sleeve is then used to concentrically couple the wrist to the spring coil. The heat shrink-tubing must not interfere with the wrists' notches, as this will affect its bending capability, otherwise it should be removed and re-applied. Next, we cut the optical fiber to length (for our tests, we used a fiber approximately 1-meter in length) using an optical fiber cleaver. Approximately 4 mm of the fiber cladding was removed from the tip with a wire stripper. The prepared optical fiber is then passed though the actuation unit and through the opposite side of the spring coil, and through the wrist assembly, so that the exposed fiber protrudes past the end cap to directly contact tissue. This protrusion should be

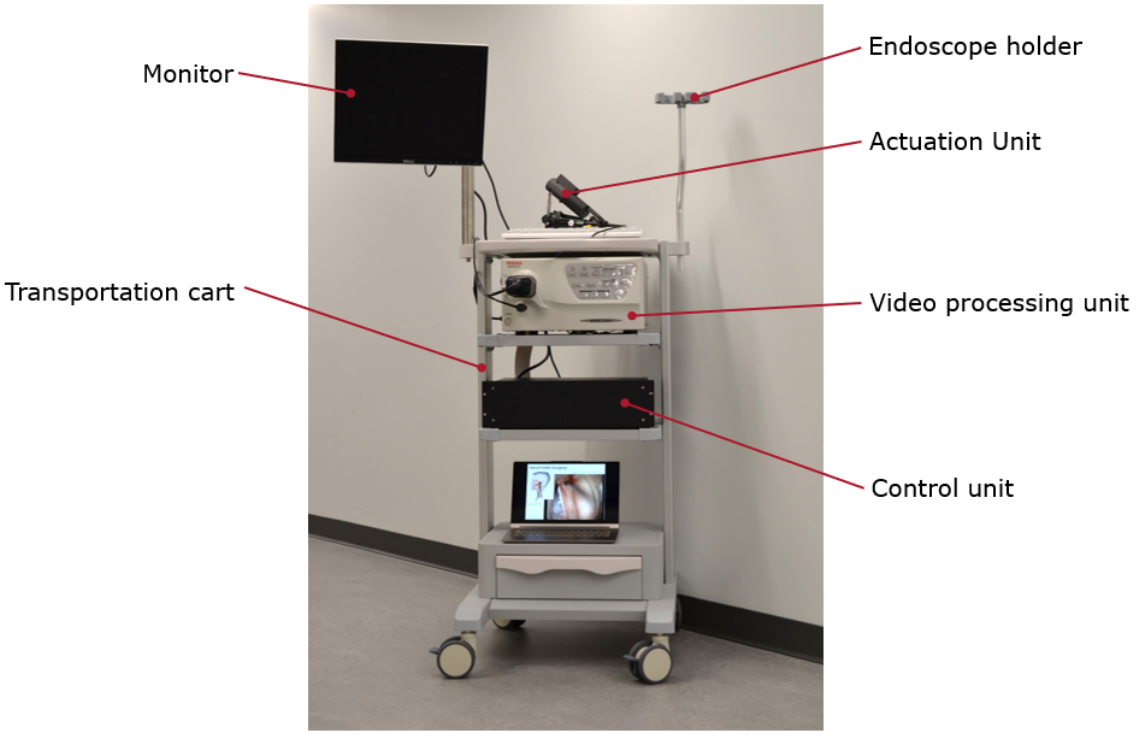

Figure 4.1: *Complete SCREAM 4 system on a medical cart.*

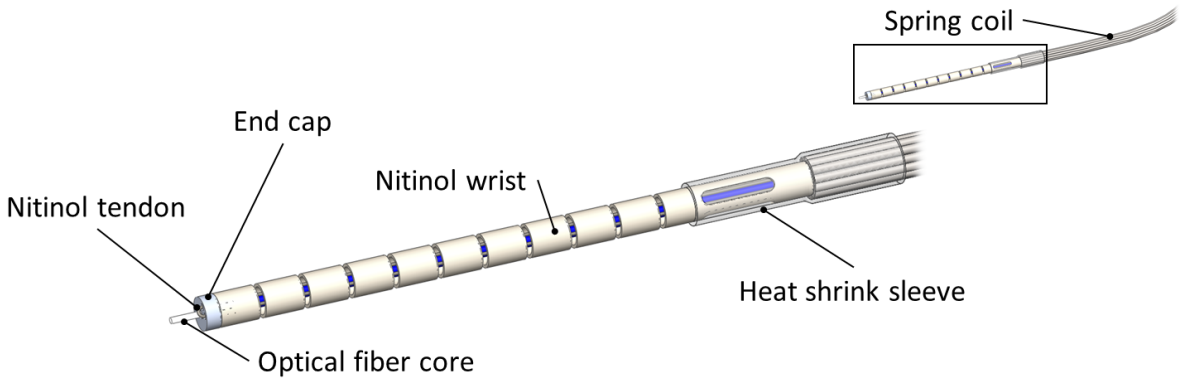

Figure 4.2: *A rendering of the steerable sheath assembly.*

no longer than approximately 2 mm, as the bare fiber is fragile. Using superglue, the fiber and Nitinol tendon are secured to the end cap. Lastly, the 'stem' of the end cap is glued to the inside of the Nitinol wrist.

This assembly, now complete, may be connected to the actuation unit. The tendon segments will pass through a channel to connect to the deflection bobbin using a set screw, while the fiber will pass through the actuation unit entirely, to be connected to a collimator and ultimately, the laser firing unit.

It is noteworthy that the order of assembly is significant, as one end of the fiber is permanently

fused to a connector. If disassembly is ever required, the tip may be submerged in acetone to dissolve the glue. While this current setup works, it is cumbersome to assemble and prepare for testing. Future work is recommended to modify the design of actuation unit to decrease assembly time, to improve our achievement and fine tune NFR 3. Moreover, superglue is not an ideal method for connecting the exposed laser fiber to the end cap, as superglue negatively affects the efficiency of the laser fiber. However, since evaluating the efficiency of the laser is out of the immediate scope of our project, we continued to use superglue as described above.

Actuation Unit For ease of assembling, we divided the actuation unit assembly into four sub-assemblies: distal core (Fig. 4.3(a)), proximal core (Fig. 4.3(b)), distal housing (Fig. 4.3(c)), and proximal housing (Fig. 4.3(d)). Though each sub-assembly requires some screws to secure their components, the four sub-assemblies connect easily to each other without the need for fasteners. Due to the precision of the 3D printers used in our development process, the printed components fit together as expected without the need for sanding or other post-printing processing.

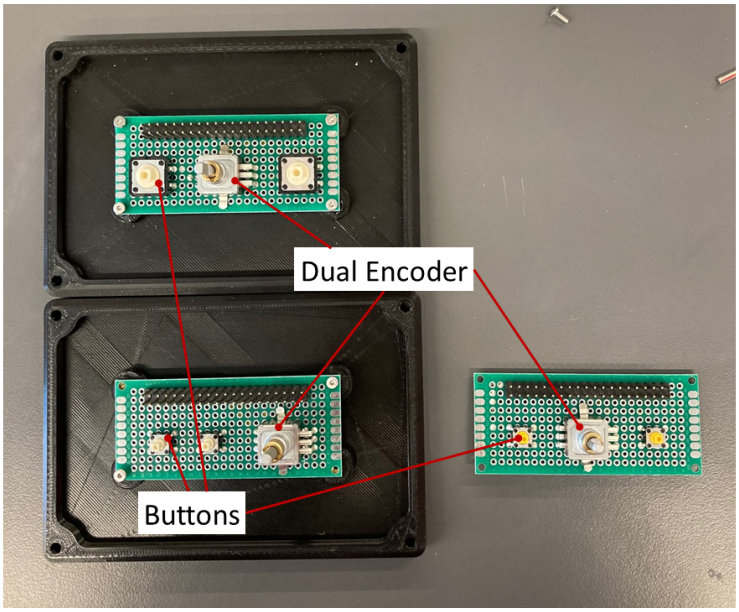

Figure 4.4: *Bench-top user interfaces created for experimentation. Each interface has a different layout and/or components for future evaluation of user-friendliness.*

User Interface While we were developing the user interface (UI), we made several bench-top UIs for testing purposes (Fig. 4.4). Each UI includes two buttons to translate the tip in and out and a dual encoder to bend and rotate the tip. The main purpose of these interfaces is to allow us to quickly actuate the tip for tests and experiments. The bench-top interfaces use different layouts and components which would allow evaluation to be conducted on the ergonomics and

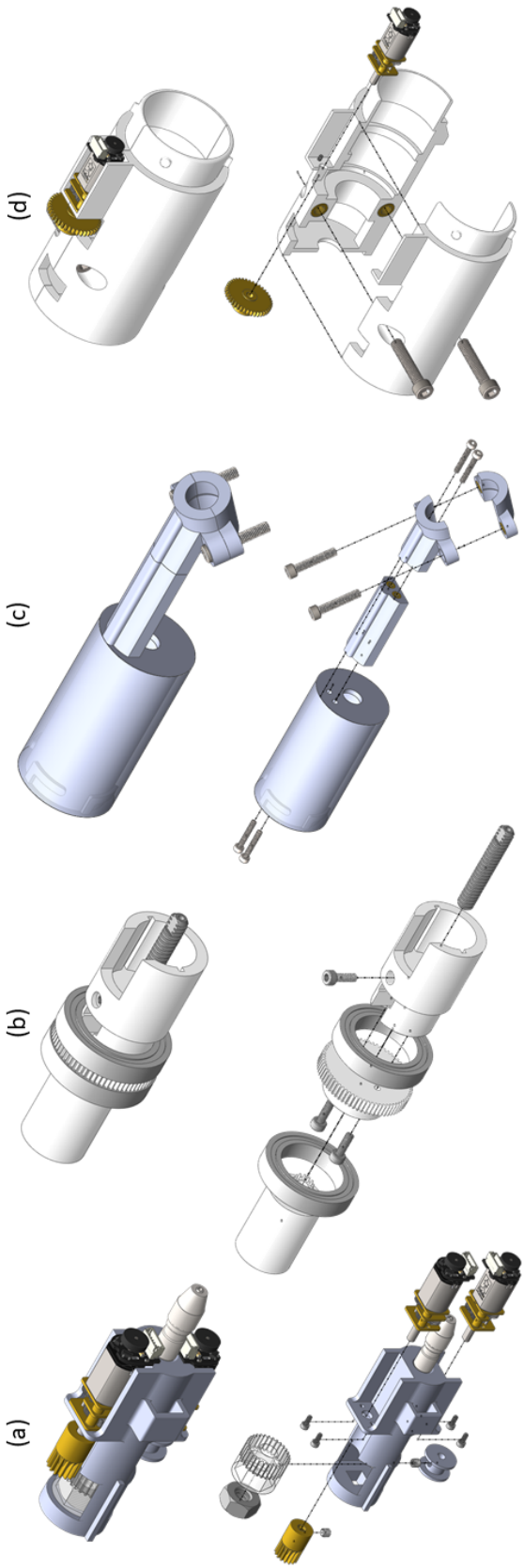

Figure 4.3: *A rendering of the four sub-assemblies of the actuation unit (top) and their corresponding exploded view (bottom).*

user experience with the design. Moreover, a benefit of the bench-top interfaces is that we would have more time to develop the mountable interfaces.

Control Unit The control unit assembly consists of two main components: assembly of the chassis, and stuffing the PCBs. The chassis is an off-the-shelf design from Hifi2000, complete with a diagram for assembly (located in Appendix C). The PCBs are custom designed by our team for this application and include a silkscreen layer which directs assembly with the aid of supporting documentation. Components such as the PCBs, transformer, and rectifiers must be affixed to the plate within the chassis. Holes should be drilled to fit the power switch, fuse holder, and IEC power socket on the back of the unit. To electrically connect the control unit to the actuation unit, an off-the-shelf 1-meter long 2x20 female-female header cable was used.

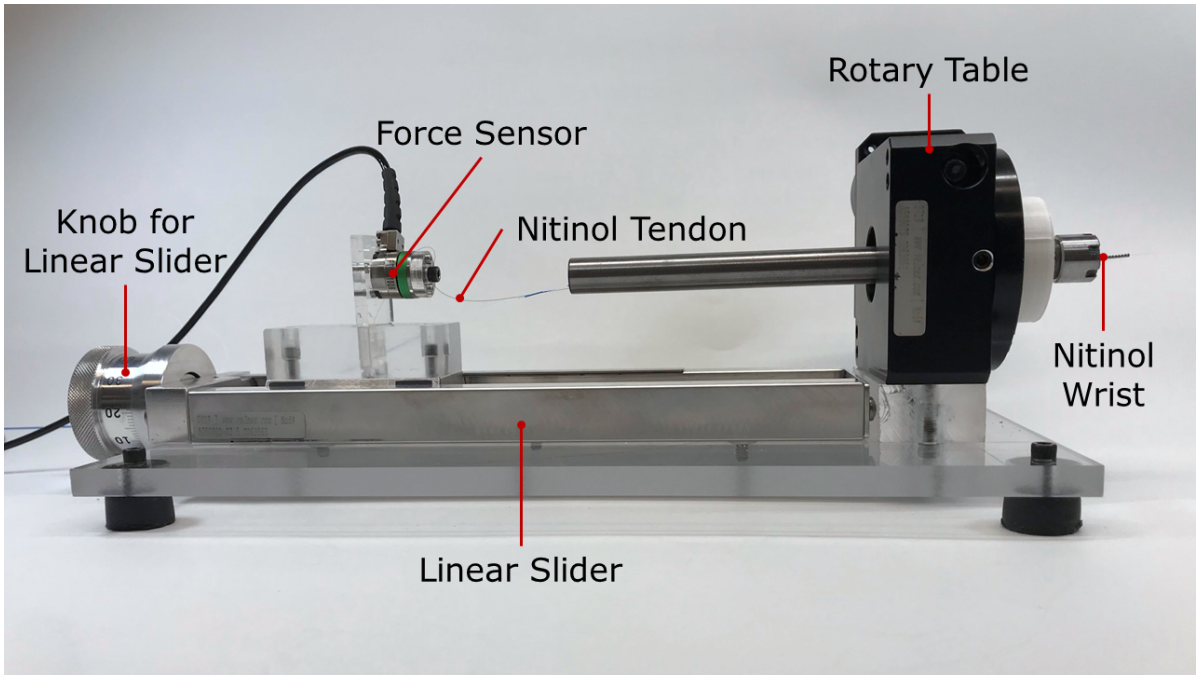

Figure 4.5: *Deflection experiment setup. The force sensor was not used for data collection in the results reported in this report.*

4.2 Mechanical Design Evaluation

With the device fabricated, we determined it was necessary to evaluate its performance against the design requirements mentioned previously. Mechanically, we would like to understand the behavior of the end effector, i.e., the Nitinol wrist. To do so, we designed experimental protocols to evaluate the physical effects of the actuation unit and steerable sheath assembly.

Deflection Experiment Setup

For the deflection experiment, we used the custom experimental setup shown in Fig. 4.5. To prepare this setup, the steerable wrist assembly was built without the optical fiber. The base of the wrist was secured to the collet, and the tendon was passed through the channel and connected to a linear slide. To capture the poses of the sheath assembly, we used a camera and lighting setup which was placed over the assembly, parallel to the bending plane.

4.2.1 Deflection Degree of Freedom

Rationale The main goal of this set of experiments was to evaluate the wrist's behavior against FRs 2 and 3. Another goal was to determine a model to describe the wrist that we could use in a simulation environment to conduct further studies.

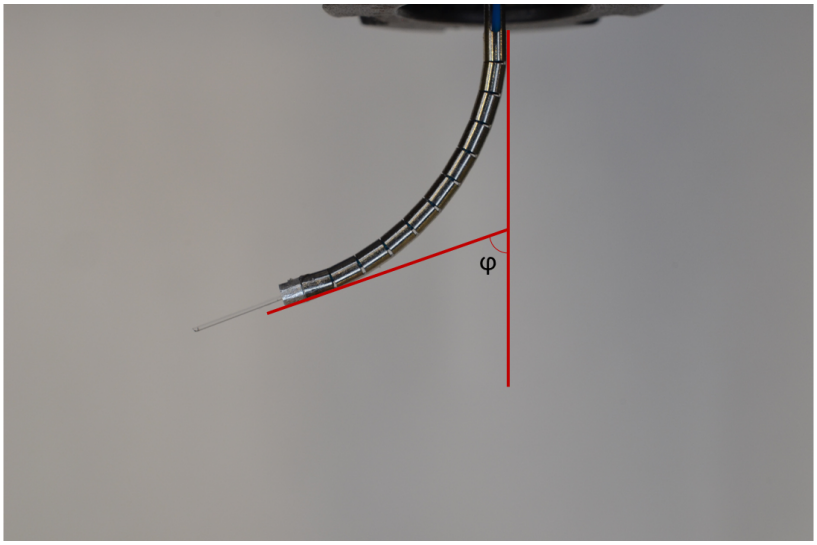

Figure 4.6: *Deflection characterization experiment image.*

Method The linear slide was jogged in increments of 0.2 mm, and the pose of the wrist was photographed after each movement. The photographs were analyzed with a custom MATLAB (The Mathworks, Natick, MA, USA) script, and the deflection angle, φ in Fig. 4.6, at each increment was measured. This process was performed for a total of five trials. The results are shown in Fig. 4.7.

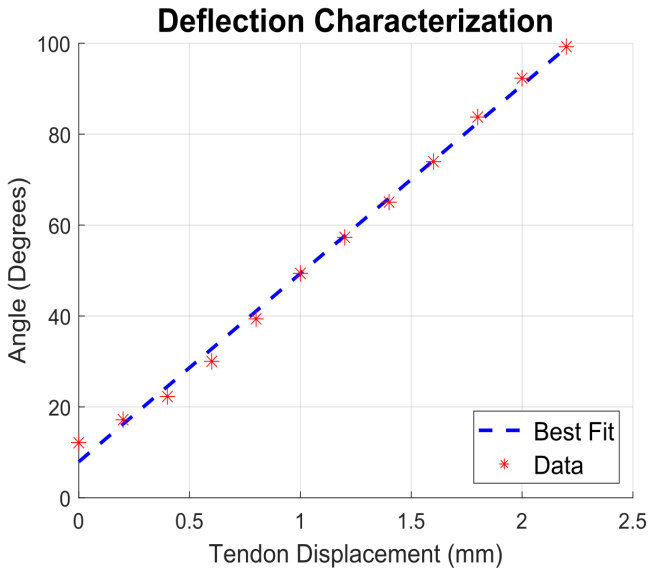

Figure 4.7: *Results of the kinematics evaluation experiments.*

Results The results in Fig. 4.7 shows that the wrist can bend up to 90° and beyond, satisfying FR 2. Though we did not obtain a measurement for bending radii, the wrist we used was

previously evaluated by SCREAM 3 as satisfying FR 3.

Beyond the achievement of the two FRs, we noticed that the relationship between the deflection angle and tendon displacement is linear. The standard deviation for the five trials was less than 1° for all values of tendon displacement. This result helped us understand the behavior of the Nitinol wrist to better control its position in future development.

Rotation and Translation Experiment Setup

For the rotation and translation experiments, we used the custom experimental setup shown in Fig. 4.8. To prepare this setup, we place the actuation unit and the endoscope on their respective

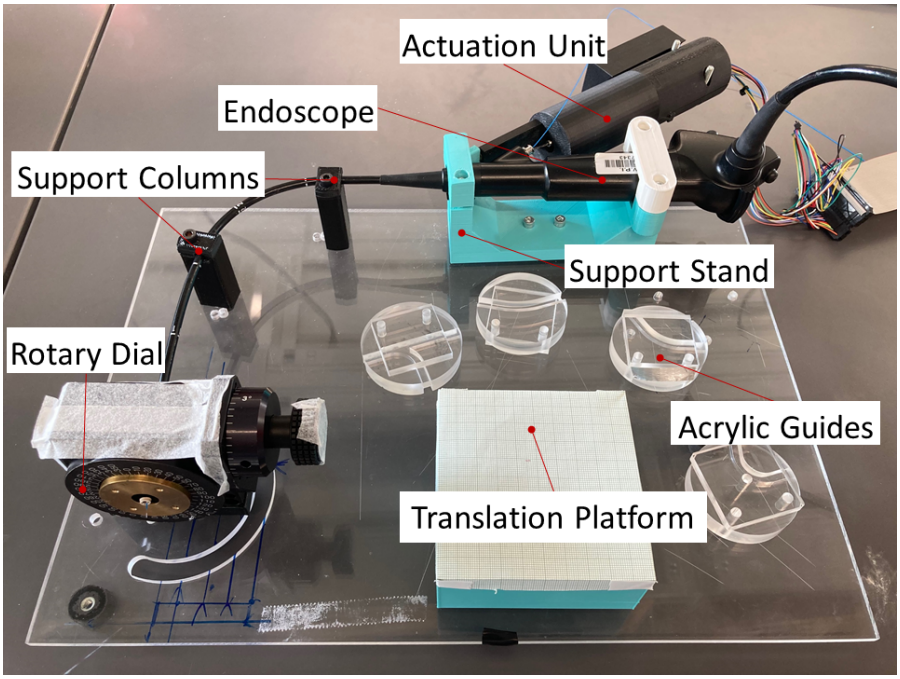

Figure 4.8: *Experiment setup used to evaluate the rotation and translation degrees of freedom.*

holders. The flexible tip of the endoscope is then passed through the two support columns. The locations of the columns help define a predetermined path for the endoscope that would mimic its pose during an office-based procedure [3]. The distal end of the flexible tip is then placed into a rotary dial (for rotation setup) or onto a platform (for translation setup). To capture the poses of the sheath assembly, we used a camera and lighting setup which was placed in front / over the assembly.

Unlike the deflection experiment which was actuated by jogging the linear slide in 0.2 mm increments, the poses for the rotation and translation experiments are controlled by the motors within the actuation unit. The equations to determine the number of encoder pulses necessary to rotate a specific amount / travel a specified distance are given in (4.1) and (4.2), respectively. Furthermore, because it is unlikely that the desired rotation / displacement will output an integer

value, the encoder pulse value will be rounded to the nearest integer. Then, the equations can be solved in reverse to find the true angle / distance the motors will set the pose to. The code we developed for control of the motors operates within an error of ±3 encoder pulses.

$$\text{motor gr} \times \text{encoder pulses per rotation} \times \text{transmission gr} \times \frac{\text{desired angle}}{360} = \text{encoder pulses} \tag{4.1}$$

$$\text{motor gr} \times \text{encoder pulses per rotation} \times \text{transmission gr} \times \frac{\text{desired distance}}{\text{lead screw thread spacing}} = \text{encoder pulses} \tag{4.2}$$

* gr = gear ratio

4.2.2 Rotation Degree of Freedom

Rationale This set of experiments aims to evaluate the end effector's performance against FRs 5, 6, and 7. Specifically, we want to understand if the new spring coil improves the rotation ratio and avoids snapping behavior.

Method In this experiment, we would like to obtain the input rotation angles at the motor shaft and the resulting output angles at the wrist. For each direction (clockwise and counter-clockwise), we ran five trials, rotating the wrist in increments of 10° for the input angle until at least 360° was observed for the output angle. After each increment, its pose was photographed, then later imported into ImageJ (U. S. National Institutes of Health, Bethesda, Maryland, USA) to determine the output angle using the angle and scale measurement tools. A raw image from the experiments is shown in Fig. 4.9. The results of this experiment are included in Fig. 4.10.

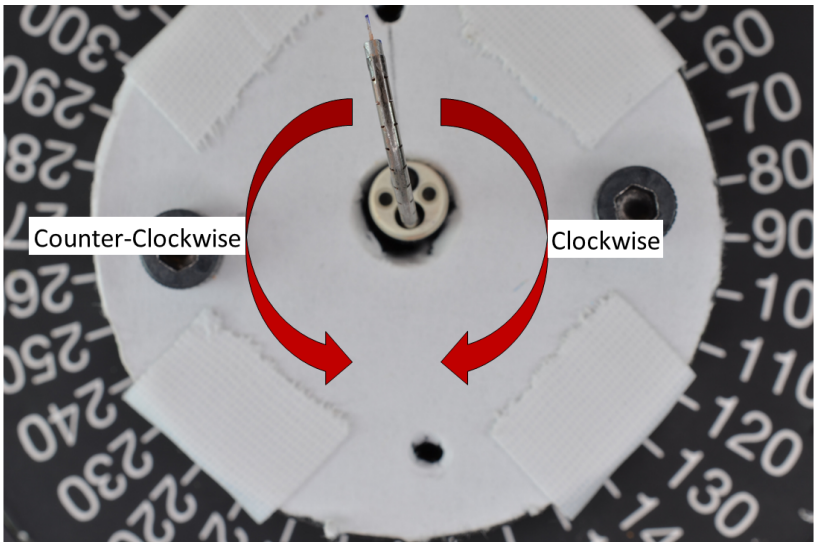

Figure 4.9: *Rotation characterization experiment.*

The rotational DoF uses a motor with a 298:1 gear ratio, and a transmission ratio of 7:4. Given the increment of 10° , the following values (shown in equation 4.3) are substituted into equation 4.1, resulting in an encoder pulse value of 41, when rounded. The resultant rotation is 10.04° . Incorporating the error bounds results in each rotation increment being between 9.306° and 10.776° .

$$280/1 \times 3 \times 7/4 \times \frac{10°}{360°} = 40.833 \text{ encoder pulses} \tag{4.3}$$

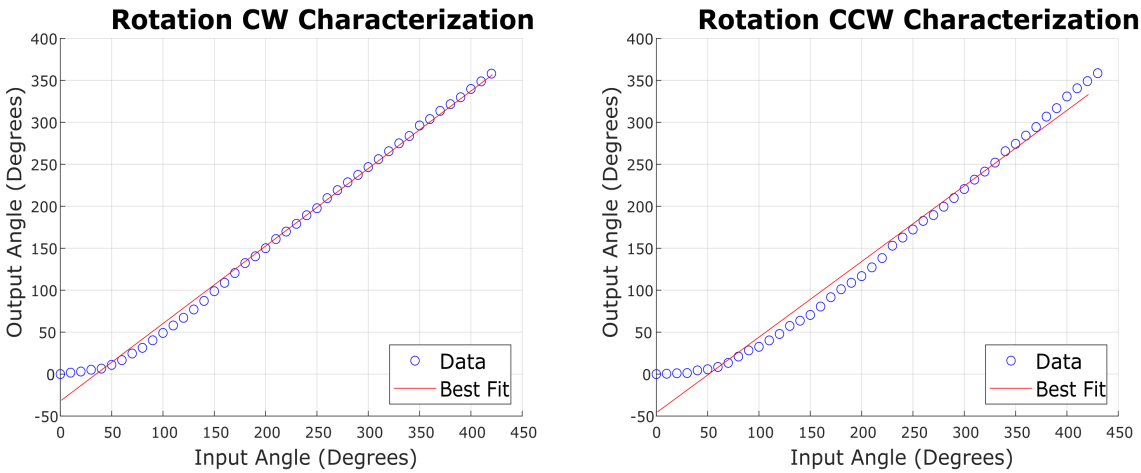

Figure 4.10: *Rotation data with hysteresis.*

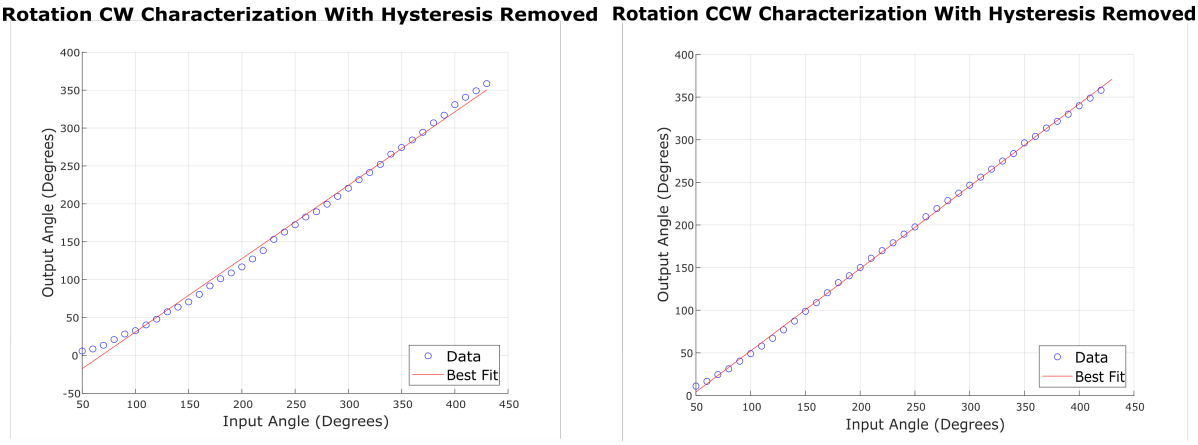

Figure 4.11: *Rotation data without hysteresis.*

Results In the rotation experiments, the wrist tip rotated more than 360° both in the CCW and CW directions, satisfying FR 5. We observed that the DoFs were successfully decoupled as the end effector did not translate or bend during these experiments, satisfying FR 7.

Fig. 4.10 shows the results from the rotation experiment for the CW and CCW trials with hysteresis. We found the CW ratio of output to input angle (i.e., the gradient of the best fit line in

Fig. 4.10, left) to equal 0.92 and the CCW ratio of output to input angle (i.e., the gradient of the best fit line in Fig. 4.10, right) to equal 0.90.

Fig. 4.11 shows the results from such experiments without hysteresis. To do this, we removed the first 5 iterations of the device's movement. We found the CW ratio of output to input angle (i.e., the gradient of the best fit line in Fig. 4.11, left) improved to 0.97 and the CCW ratio of output to input angle (i.e., the gradient of the best fit line in Fig. 4.11, right) improved to 0.96. Both sets of these numbers show improvement over SCREAM 3's CW ratio of 0.97 and CCW ratio of 0.42 [3]. These results show the increased torsional rigidity of our device over SCREAM 3.

Our experimental process for the rotational DoF was to run all trials consecutively, alternating between clockwise and counterclockwise directions. The impact of choosing this methodology is that it reveals the hysteresis of the system as it is changing directions as shown in Fig. 4.10. Most prominently are the effects of the spring coil as it begins rotating in the opposite direction. Nonetheless, characterizing such hysteresis is critical to understanding the behavior of the end effector, and thus being able to compensate for it. The error introduced from the motor provides no significant impact on our results.

4.2.3 Translation Degree of Freedom

Rationale This set of experiment aims to evaluate the wrist's performance against FR 4. We also wanted to understand if the spring coil was compressionally rigid. Though this rigidity is not a design requirement, understanding the spring coil axial behavior would allow us to predict the tip movement and understand the stored energy within the coil for potential safety consideration. The availability of this data would also allow future works to quantitatively compare their improvements to our design.

Method In order to test the translation DoF, a translation experiment was run with the setup in Fig. 4.8, using a grid of 1 mm as a background. For each translation direction (in and out), five trials were completed. The input displacement of each translation increment was 0.5 mm. After each actuation, the wrist's position was photographed. A raw image is shown in Fig. 4.12(c). The experimental distances of each device iteration were analyzed using ImageJ's (U. S. National Institutes of Health, Bethesda, Maryland, USA) segment line and scale measurement tools.

The translational DoF uses a motor with a 380:1 gear ratio, and a transmission ratio of 2:1. Given the desire to move 0.5 mm and the lead screw thread spacing of 1.6 mm, the following values (shown in equation 4.4) are substituted into equation 4.2, resulting in an encoder pulse value of 713, when rounded. The resultant rotation is 0.500 mm. Incorporating the error bounds results in each rotation increment being between 0.498 mm and 0.502 mm.

$$380/1 \times 3 \times 2/1 \times \frac{0.5 \text{ mm}}{1.6 \text{ mm}} = 712.5 \text{ encoder pulses} \tag{4.4}$$

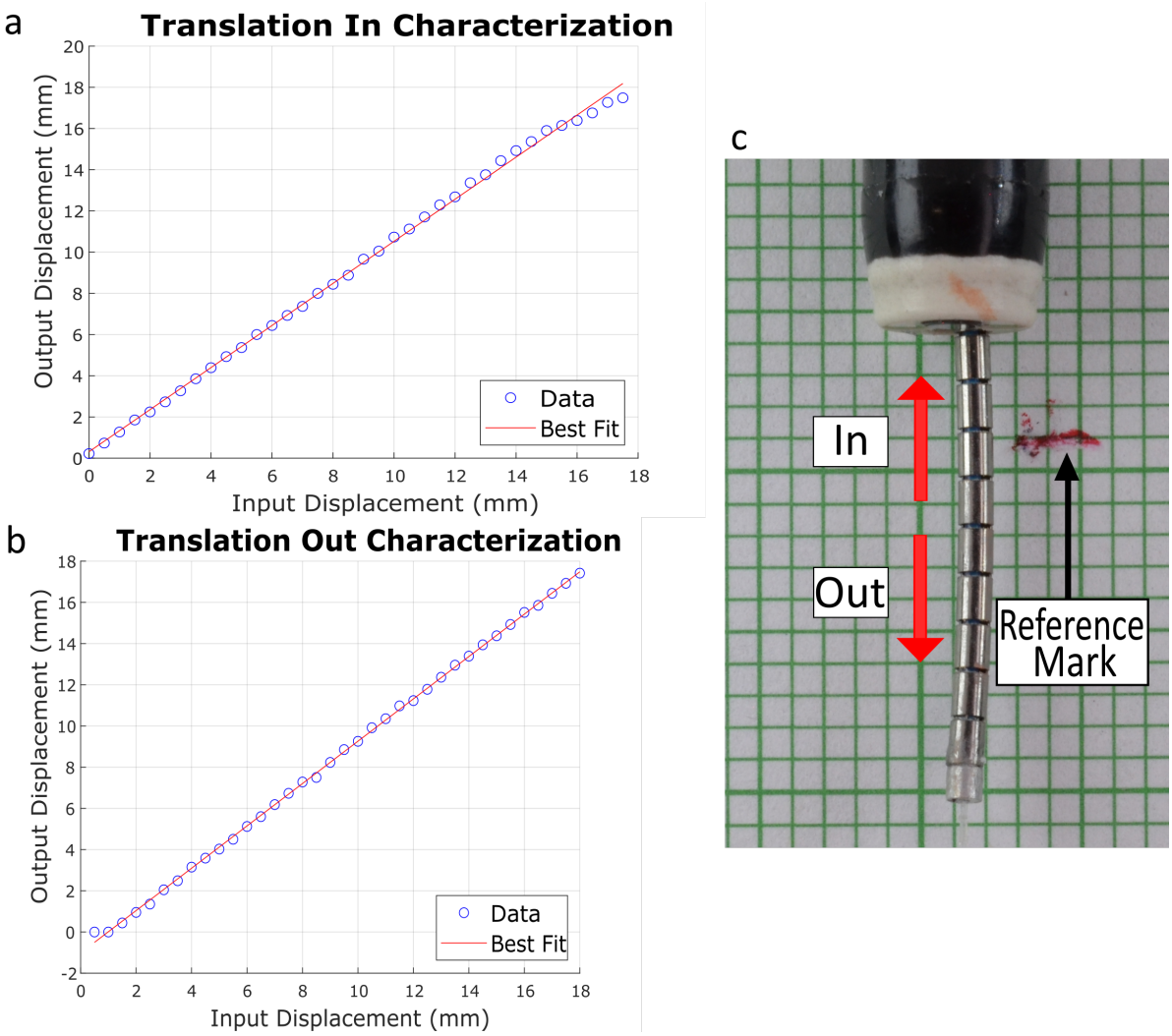

Figure 4.12: *Translation characterization experiment. Graphs (a) and (b) show the output displacement versus input displacement for translation in and out, respectively. (c) Shows the direction of tip movement.*

Results In terms of meeting FR 4, the maximum output displacement is about 17 mm, satisfying the range of 10-20 mm for translation. Moreover, Fig. 4.12(a) and (b) show a strong linear relationship between the input displacement of the wrist versus its output displacement. The slopes of the output versus input displacements are 1.021 for translation in and 1.028 for the translation out with low variance and standard deviation levels. This result suggests that the spring coil has a high compressional rigidity. The error introduced from the motor provides no significant impact on our results.

4.3 Reachable Workspace Verification

We performed a simulation study to visualize and measure the amount of tissue that can be accessed with our new steerable fiber. The goal of this simulation was to visualize and measure the amount of tissue that can be accessed by the laser using a steerable fiber compared to a traditional straight fiber (no angled laser firing) and to help us select the optimal wrist parameters for manufacturing. The simulations used the same methods introduced earlier in Chapter 2. Similarly to the angle firing experiment, we ran the simulation for 10000 points first with no wrist activation, then with Wrist 2 for each larynx model. Table 4.1 displays the simulation results for Larynges 1 and 2 with no wrist and with Wrist 2. Fig. 4.13 depicts the accessible tissue with a traditional fiber and with Wrist 2. While Wrist 1 proved to allow for the greatest reachable tissue, the physical wrist with those parameters had broken, so we proceeded with the next best option, Wrist 2, for the assembly of the device.

As seen in the raw results from Table 4.1, the area of reachable tissue for both laryngeal models increased from approximately 9 cm^2 to at least 20 cm^2, at least doubling the predicted surgical access with the wrist. Moreover, the vocal folds that tend to be difficult to reach in office-based surgery are better covered with the steerable wrist. The significance of tissue coverage can vary depending on the CT scan configurations and anatomical differences of the individual larynx models, which is why percentages were calculated in Table 4.1.

Table 4.1: *Wrist study results.*

	Traditional Fiber		**Steerable Fiber**	
Larynx	**cm^2**	*%*	**cm^2**	*%*
L1	8.99	21.37	22.22	57.79
L2	8.51	23.13	20.49	55.65
Mean		22.25		54.22
Std		0.012		0.020

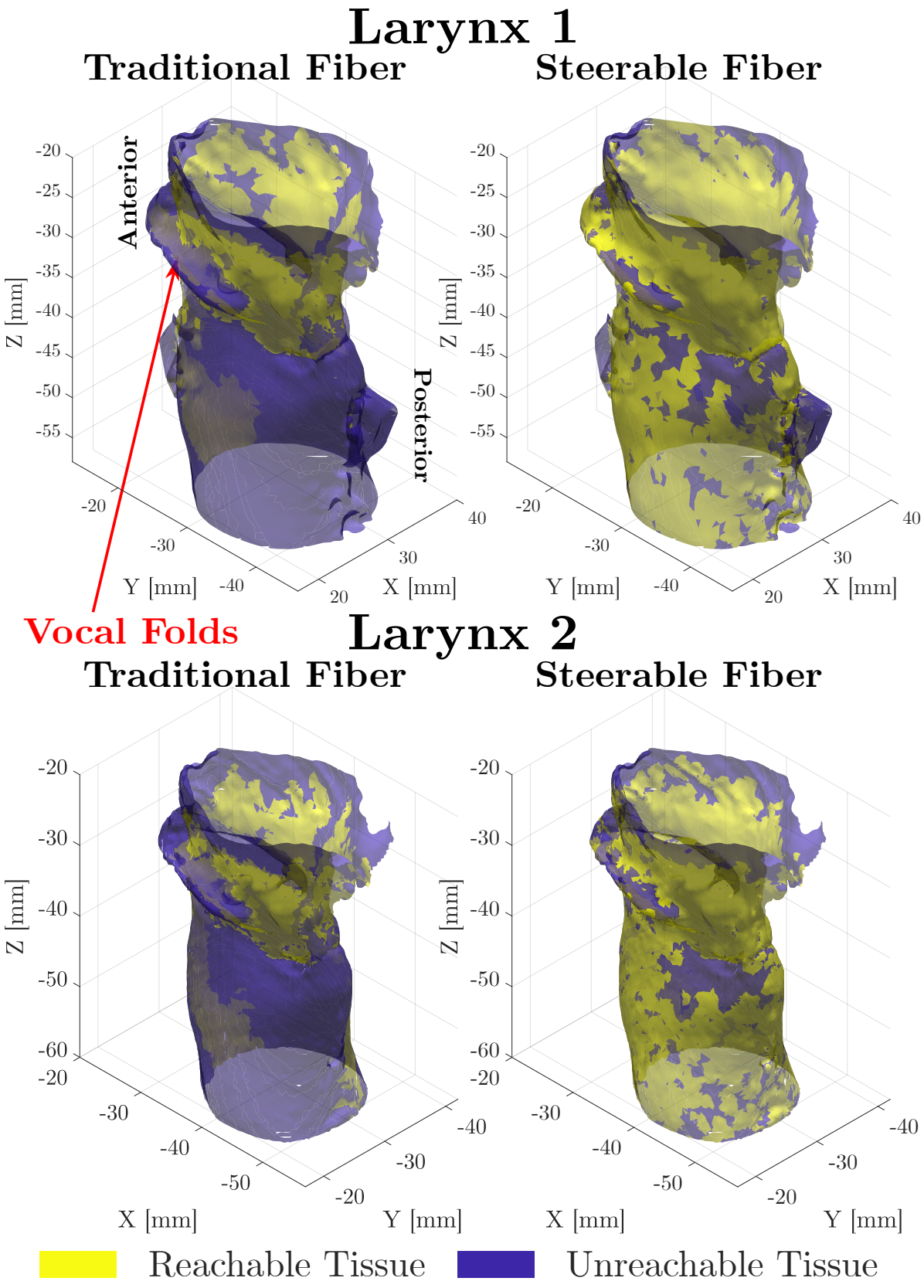

Figure 4.13: *Wrist simulation results.*

CHAPTER 5

DISCUSSION AND FUTURE WORK

The goal of this project was to create a needle-sized continuum robot to enhance surgical access in office-based endoscopic laser surgery of the larynx. Overall, this was accomplished by designing and integrating our device and experimenting with it both physically and in simulation.

5.1 Advancement over Past SCREAM Projects

In this project, we expanded the side-laser firing study performed by Chan *et al.* [2] to include seven larynx models instead of just two. This study concluded that a side-firing angle of 90° would greatly increase the tissue accessibility of the endoscope. Knowing this, we were able to focus on a couple wrist types that are each capable of bending 90° and further refining the design based on the vaster anatomical coverage provided with the wrist.

Moreover, the rotational decoupling of the steerable fiber was improved, and a 90° deflection angle was achieved. We also solved the issue of cable tangling by using a slip ring. We integrated our system on a medical cart in order to fulfill the requirement of ease of integration into the surgical environment. The control unit organizes and centralizes the cables allowing for a smooth integration on the medical cart.

Our device is ready for verification and validation through cadaver experiments, for which we created a protocol. It is easier to hygienically reprocess our device than previous prototypes due to its compactness and organization.

5.2 Limitations

In our simulation studies, we faced two main limitations. The first limitation is due to the nature of the larynx models. Because they were created from micro-computed tomography scans of

cadaver models, the anatomy of the larynges were fixed whereas in-office patients' tissues are not fixed. The second limitation is that in our studies we only included 7 larynx models which may not be representative of the anatomical variability of a wide population. However, while this is true, it is difficult to obtain such larynx models.

We faced some limitations when manufacturing parts for the device. Highly customized products such as the spring coil, wrist, and PCBs had long lead time waits. Some components in our prototype were not in our intended design, but they were more readily available and still did the job.

5.3 Future Work

5.3.1 Cadaver Study

In the future, our device can be further validated by performing preclinical testing on cadaver specimens. This section describes the preparation we completed in order to run the cadaver studies. The experiments will be performed in the anatomy lab of the University of Massachusetts Memorial Medical Center - University Campus. After consulting with the project clinical advisor, Dr. Thomas Carroll, and his collaborator Dr. Eliana DeVore, we created an experimental protocol shown in Appendix B. The protocol was created from the knowledge that we would use whole fresh cadaver larynges for the experiments. To sanitize the device after the experiments, we will use glutaraldehyde (GA). The glutaraldehyde will be used to clean the spring coil and the actuation unit will be sanitized with a 70% isopropyl alcohol solution.

5.3.2 Additional Future Work

While we explored two different types of simulation studies, shown in Section 2, there is still a wide variety of experimentation that could be studied. Future simulation experimentation could involve varying the dq further, looking at other endoscope and wrist configurations inside the larynx, increasing the number of models used, and studying other side-firing angles besides 45°, 70°, and 90°. Future work could also include comparing the two studies included in Section 2 to see if angled fibers or steerable wrists provide greater anatomical coverage.

More work is also needed to develop a user interface that provides the physician with ergonomic single-handed manipulation. In future works, more methods to optimize the design of the steerable sheath to increase tissue reachability could be explored. Regarding NFR 3, we recommend future teams to conduct a time study on how long it takes to connect the steerable sheath assembly to the actuation unit, for quick pre-procedure preparation. The spring coil collet is a start, but changes to the actuation unit design are needed to further improve the achievement on NFR 3. Future work also includes finding a way to attach the end-cap to the laser fiber with a different adhesive than superglue as the current method is not optimal for the laser fiber's firing efficiency.

CHAPTER 6

BROADER IMPACTS

6.1 Engineering Ethics and Regulations

This project was conducted in compliance with core biomedical ethics principles, including confidentiality, beneficence, and justice, and laboratory safety requirements [16]. Safety was of utmost importance during all fabrication and testing procedures. The use of lasers is a safety aspect which was handled with care by all researchers and physicians. Only laser-trained individuals used the laser in our laser approved laboratory. Additionally, Blood-borne Pathogens Biosafety Training was pursued by each project member and the main faculty advisor, Prof. Fichera, through the WPI Environmental Health and Safety Office in order to ensure proper understanding of laboratory practices and how to limit possible transmission of hazardous biological contaminants from the tissue we would work with. This led the team to conduct further research and seek the professional advice of a biosafety officer as well as our clinical collaborators on how to effectively clean the device in between uses.

6.2 Global Impact

Our device provides larynx surgeons who use a typical flexible endoscope a system for more refined steering of the laser fiber to access more locations in the larynx. This will allow for a swifter procedure, reduce procedure time, and widen the opportunity for patients to be treated via office-based laser surgery. It is well-known that topical anesthesia has fewer complications than general anesthesia. Cottrell and Hartung found that the elderly have a greater risk after surgery because their recovery systems are diminished. Because of this, they have less resilience to neurological challenges such as anesthetic neurotoxicity. Cottrell and Hartung inferred that these findings may contribute to the fact that elderly patients experienced an increased rate of

brain atrophy after receiving surgery [17]. In-office laser surgery is safer for elderly patients since regional anesthesia is used rather than general anesthesia. Our project would impact global communities, improving the quality of life for candidates for laryngeal surgery and getting closer to helping the 1 in 40 people affected by laryngeal tumors worldwide [6].

6.3 Economic Factors

One of the common benign laryngeal tumors is laryngeal papillomatosis, or rapid recurrent papillomatosis (RRP). Currently, there is no cure for RRP. Patients with RRP require numerous surgeries per year to remove their rapidly growing laryngeal tumors [7]. Rees et al. discovered that performing surgery in-office versus in a tradition operating room setting saves more than $5000 on average [18]. This decrease in cost benefits patients, caretakers, and insurance companies and has the potential to improve the quality of life for many people with RRP. Working within the constraints of office-based procedures, our steerable device makes it easier to perform and receive such surgical treatment, making it a more appealing option both for its improved non-invasive features and similar cost to current endoscopic treatment.

The mass production of the device would be relatively inexpensive as many components for the control unit and actuation unit can be bought off-the-shelf. The sheath assembly would be the main direct expense to the patient due to the likelihood of it needing to replaced between procedures.

BIBLIOGRAPHY

[1] A. T. Hillel, M. C. Ochsner, M. M. Johns III, and A. M. Klein, "A cost and time analysis of laryngology procedures in the endoscopy suite versus the operating room," *The Laryngoscope*, vol. 126, no. 6, pp. 1385–1389, 2016.

[2] I. A. Chan, J. F. d'Almeida, A. J. Chiluisa, T. L. Carroll, Y. Liu, and L. Fichera, "On the merits of using angled fiber tips in office-based laser surgery of the vocal folds," in *Medical Imaging 2021: Image-Guided Procedures, Robotic Interventions, and Modeling*, vol. 11598, p. 115981Z, International Society for Optics and Photonics, 2021.

[3] P. Abell, S. Johnson, S. Liu, and Z. Xu, "Scream 3.0: Super-elastic continuum robot for endoscopic articulation and manipulation," 2021.
MQP Report.

[4] L. Bailly, T. Cochereau, L. Orgeas, N. H. Bernardoni, S. R. Du Roscoat, A. Mcleer-Florin, Y. Robert, X. Laval, T. Laurencin, P. Chaffanjon, *et al.*, "3d multiscale imaging of human vocal folds using synchrotron x-ray microtomography in phase retrieval mode," *Scientific reports*, vol. 8, no. 1, pp. 1–20, 2018.

[5] S. M. LaValle, *Planning algorithms*.
Cambridge university press, 2006.

[6] J. H. Hah, S. Sim, S.-Y. An, M.-W. Sung, and H. G. Choi, "Evaluation of the prevalence of and factors associated with laryngeal diseases among the general population," *The Laryngoscope*, vol. 125, pp. 2536–2542, July 2015.

[7] S. Katsenos and H. D. Becker, "Recurrent respiratory papillomatosis: a rare chronic disease, difficult to treat, with potential to lung cancer transformation: apropos of two cases and a brief literature review," *Case reports in oncology*, vol. 4, no. 1, pp. 162–171, 2011.

[8] K. M. Tibbetts and C. B. Simpson, "Office-based 532-nanometer pulsed potassium-titanyl-phosphate laser procedures in laryngology," *Otolaryngologic Clinics of North America*, vol. 52, pp. 537–557, June 2019.

[9] A. G. Del Signore, R. N. Shah, N. Gupta, K. W. Altman, and P. Woo, "Complications and failures of office-based endoscopic angiolytic laser surgery treatment," *Journal of voice : official journal of the Voice Foundation*, vol. 30, no. 6, pp. 744–750, 2016.

[10] K. O'Brien, Z. R. Boyer, B. G. Mart, C. T. Brolliar, T. L. Carroll, and L. Fichera, "Towards flexible steerable instruments for office-based laryngeal surgery," in *2019 Design of Medical Devices Conference*, American Society of Mechanical Engineers, Apr. 2019.

[11] J. Bartone, J. d'Almeida, A. Gulotta, and N. Pacheco, "Scream 2.0: Super-elastic continuum robot for endoscopic articulation and manipulation." `https://digital.wpi.edu/concern/student_works/g158bk835?locale=en`, 2020.
MQP Report.

[12] A. J. Chiluisa, N. E. Pacheco, H. S. Do, R. M. Tougas, E. V. Minch, R. Mihaleva, Y. Shen, Y. Liu, T. L. Carroll, and L. Fichera, "Light in the larynx: a miniaturized robotic optical fiber for in-office laser surgery of the vocal folds," 2022.

[13] A. G. Del Signore, R. N. Shah, N. Gupta, K. W. Altman, and P. Woo, "Complications and failures of office-based endoscopic angiolytic laser surgery treatment," *Journal of Voice*, vol. 30, no. 6, pp. 744–750, 2016.

[14] P. Cignoni, M. Callieri, M. Corsini, M. Dellepiane, F. Ganovelli, and G. Ranzuglia, "MeshLab: an Open-Source Mesh Processing Tool," in *Eurographics Italian Chapter Conference* (V. Scarano, R. D. Chiara, and U. Erra, eds.), The Eurographics Association, 2008.

[15] E. Amanov, T.-D. Nguyen, and J. Burgner-Kahrs, "Tendon-driven continuum robots with extensible sections—a model-based evaluation of path-following motions," *The International Journal of Robotics Research*, vol. 40, no. 1, pp. 7–23, 2021.

[16] G. D. Byrd and P. Winkelstein, "A comparative analysis of moral principles and behavioral norms in eight ethical codes relevant to health sciences librarianship, medical informatics, and the health professions," *Journal of the Medical Library Association: JMLA*, vol. 102, no. 4, p. 247, 2014.

[17] J. E. Cottrell and J. Hartung, "Anesthesia and cognitive outcome in elderly patients: a narrative viewpoint," *Journal of neurosurgical anesthesiology*, vol. 32, no. 1, p. 9, 2020.

[18] C. J. Rees, G. N. Postma, and J. A. Koufman, "Cost savings of unsedated office-based laser surgery for laryngeal papillomas," *Annals of Otology, Rhinology & Laryngology*, vol. 116, no. 1, pp. 45–48, 2007.

APPENDIX A

APPENDIX A: AUTHORSHIP

Section	Title	Author
	Abstract	All
	Executive Summary	All
1	Introduction	All
2.1	Simulation Methods	Rositsa Mihaleva & Emily Minch
2.2	Comparing Firing Angles	Emily Minch
3.1.1	Original Design Requirements	Hoang Do & Emily Minch
3.1.2	SCREAM 3 Achievements	Hoang Do & Rositsa Mihaleva
3.1.3	SCREAM 3 Areas of Improvement	Hoang Do & Ryan Tougas
3.2	Updated Design Requirements	Hoang Do
3.3	SCREAM 4 Design Solution	Hoang Do & Ryan Tougas
4.1	Integration	Hoang Do
4.2	Mechanical Design Evaluation	Hoang Do
4.2.1	Deflection Degree of Freedom	Ryan Tougas & Emily Minch
4.2.2	Rotation Degree of Freedom	Ryan Tougas & Hoang Do
4.2.3	Translation Degree of Freedom	Emily Minch
4.3	Reachable Workspace Verification	Rositsa Mihaleva
5.1	Advancement over Past SCREAM Projects	Emily Minch
5.2	Limitations	All
5.3	Future Work	Emily Minch
6.1	Engineering Ethics and Regulations	Rositsa Mihaleva
6.2	Global Impact	Rositsa Mihaleva & Emily Minch

6.3	Economic Factors	Rositsa Mihaleva & Emily Minch

APPENDIX B

APPENDIX B: CADAVER PROTOCOL

Materials:

- Fresh cadaver larynges
- PVC pipe contraption
- Channel scope
- Tower with processor
- Light source
- Device
- Control unit
- Laser cart
- Surgical tools:
  - Needle driver
  - Suture scissors
  - Metzenbaum scissor
  - Hemostat
  - 0-Silk suture

Protocol:

1. Mount the larynx on the PVC pipe contraption.
2. Clean off excess tissue on the larynx.
3. Turn the device on (control supply unit, video processing unit, laser system, etc.).
4. Place the device into the larynx.
5. Maneuver the wrist into position.
6. Fire the laser.
7. Repeat steps 4-5 until all desired locations of the larynx have been reached.

APPENDIX C

APPENDIX C: CONTROL UNIT SCHEMATICS

Our control unit contains two printed circuit boards (PCB), tasked with separately handling the control circuitry and power conversion. The control circuitry (Fig. C.1) is separated into three main sections which all interface with the microcontroller: the connector, the motor output stage, and the button processing stage. The connector is where the cable of the actuation unit plugs into, and routes signals to the other stages of the control circuitry. The exception to this are the motors' encoder signal outputs, which require no additional processing and may be passed directly to the microcontroller. The motor output stage contains three SN754410NE H-Bridges, capable of driving up to six motors concurrently. This stage receives input from the microcontroller, regarding which motor to drive, and for how long. Access to the chip enables are also given, allowing for the option of using pulse-width modulation. Each motor is also fused, providing protection.

The button processing stage takes the thirteen button inputs, and passes them though a de-bouncing circuit and Schmitt-Trigger (SN74HC14AN) before presenting this output signal to the microcontroller. Because encoders functionally act as two buttons, a single encoder would occupy two signal inputs. All inputs are expected to be digital (high or low), not supporting the input of analog devices, such as a potentiometer.

The design of our power supply (Fig. C.2) was adapted from an existing design by Team dA at diyaudio. Functionally, this design acts as two separate supplies that share a common ground. In our design configuration these both output 6V, but can be modified by changing the rectified input signal. In the 6V configuration, each rail is capable of outputting 4A without significant voltage drop, the worst-case-scenario of 25 percent greater than the current draw of three motors at stall.

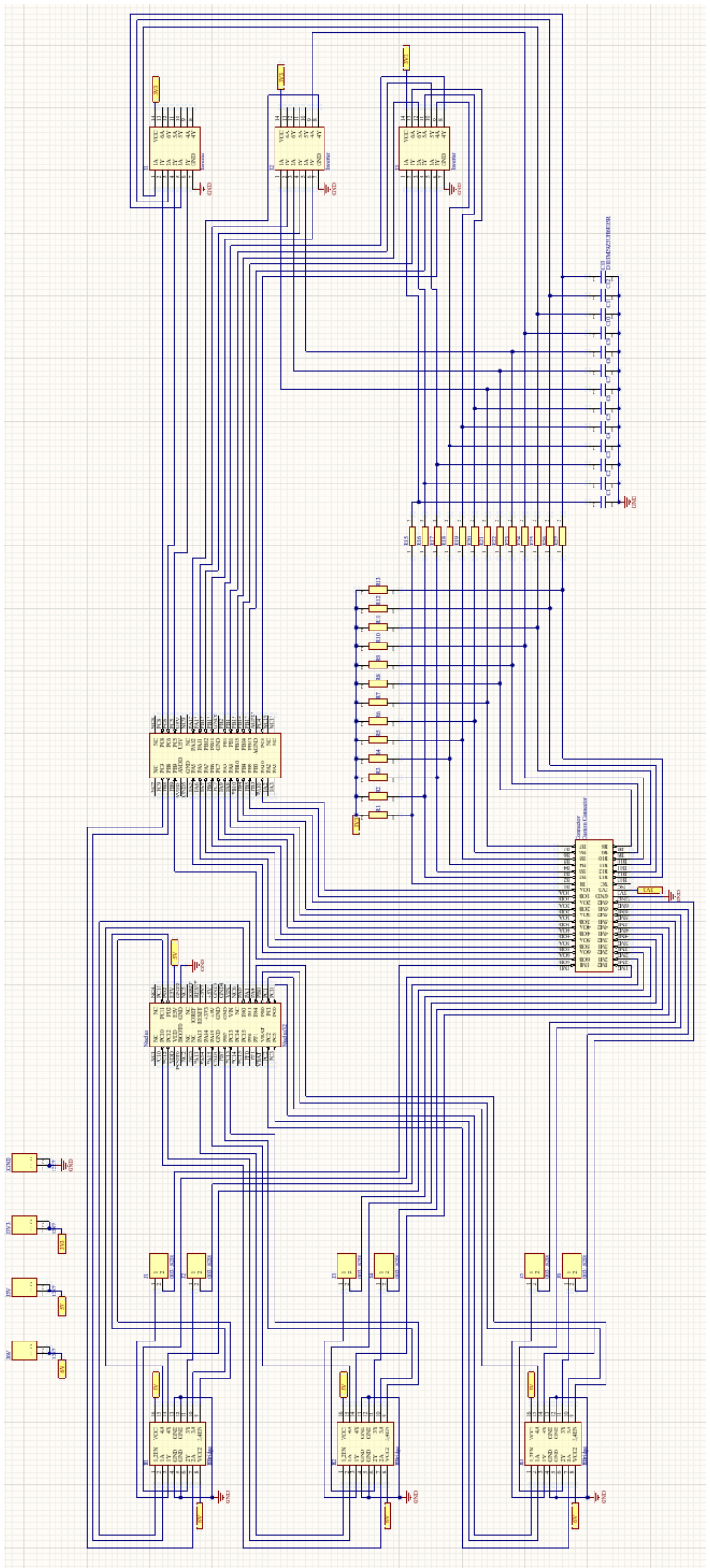

Figure C.1: *Control Circuitry Schematic*

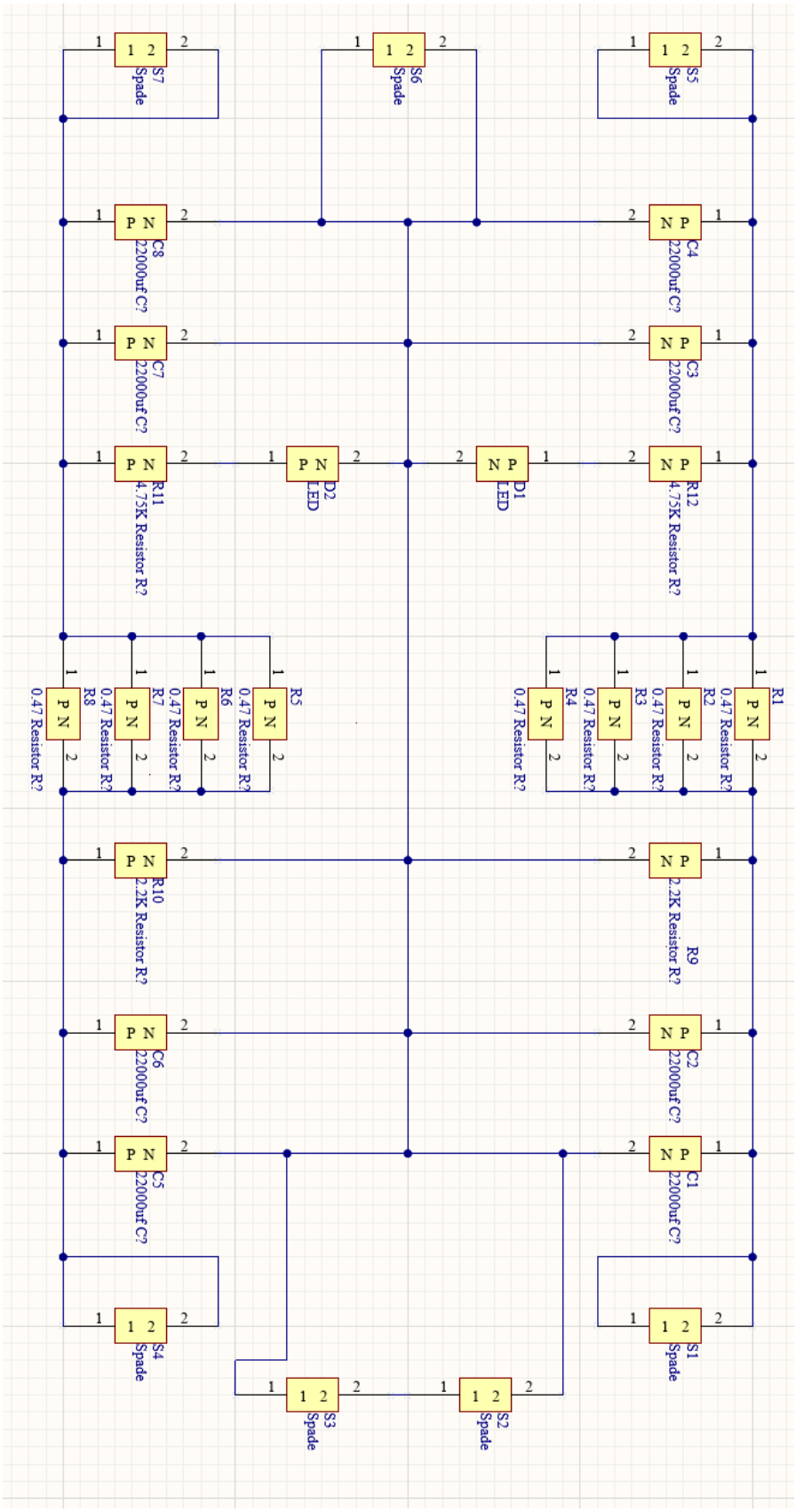

Figure C.2: *Power Supply Schematic*